PRODUCTION OF Mo-99/Tc-99m VIA PHOTONEUTRON REACTION USING NATURAL MOLYBDENUM

A Thesis

by

TALAL BADER HARAHSHEH

Submitted to the Office of Graduate and Professional Studies of
Texas A&M University
in partial fulfillment of the requirements for the degree of

MASTER OF SCIENCE

Chair of Committee,	Gamal Akabani
Co-Chair of Committee,	John W. Poston, Sr.
Committee Member,	Victor M. Ugaz
Head of Department,	Yassin A. Hassan

May 2017

Major Subject: Nuclear Engineering

ABSTRACT

The current shortage of the widely used radionuclide ^{99m}Tc has raised many concerns in the nuclear medicine industry. The shortage is caused by the outdated method of production using highly enriched uranium (HEU) and nuclear reactors. This production method is no longer feasible due to the restrictions on the use of HEU. Alternative methods of production must be addressed to ensure the uninterrupted supply of this key radionuclide. This research analyzes an alternative production method of ^{99m}Tc using an accelerator-generated ^{99}Mo, which is the parent element of ^{99m}Tc. The radionuclide ^{99m}Tc has a short half-life of 6 hours. However, ^{99}Mo, the parent nuclide has a much longer half-life of 66 hours. Usually, a medical facility receives a ^{99}Mo/^{99m}Tc generator. Technetium-99m would be obtained from the ^{99}Mo provided through chemical separation, which is conducted at the medical facilities. The main issues to be addressed include the production of ^{99}Mo using the photonuclear reaction, the containment and exclusion of unwanted decay products, ensuring the integrity of the end-product ^{99}Mo/^{99m}Tc post chemical separation, and assessing the economic feasibility of the complete strategy, including life cycle. If feasible, this production route would eliminate the use of HEU and nuclear reactors, guarantee an unwavering supply of the radionuclide at a lower cost, and assist on the regional growth of the radionuclide production industry worldwide.

ACKNOWLEDGEMENTS

I would first like to express my profound gratitude to my thesis advisor Dr. Gamal Akabani. Dr. Akabani was always available whenever I ran into a trouble spot and would not rest till it was resolved. Without Dr. Akabani's guidance and vision, this research would not have been significant. I would also like to thank Dr. Poston and Dr. Ugaz for serving as members on my committee.

Finally, I must express my very deep gratefulness to my family and friends for providing me with unfailing support and continuous encouragement throughout my years of study and through the process of researching and writing this thesis. This accomplishment would not have been possible without them. Thank you.

NOMENCLATURE

ADSR	Accelerator Driven Subcritical Reactor
Ao/As	Phase activity before/after equilibration
CFR	Code of Federal Regulations
cpm	Counts per minute
CSDA	Continuous Slowing Down Approximation
EOB	End of Bombardment
EOC	End of Cooling
HEU/LEU	Highly/Low Enriched Uranium
JANIS	Java-based Nuclear Data Information System
K_d	Partition Coefficient
MSIG	Multicolumn Selectivity Inversion Generator
NRC	Nuclear Regulatory Commission
rr	Microscopic Reaction Rate in atoms mA^{-1} s^{-1}
RR	Macroscopic Reaction Rate in atoms mA^{-1} s^{-1}
$\sigma(E)$	Microscopic Cross Section cm^2 per atom
$s(E)$	Photon Fluence Rate mA cm^{-2} s^{-1}
$T_{1/2}$	Half Life
TENDL	TALYS-based Evaluated Nuclear Data Library
USP	United States Pharmacopeia
DMF	Drug Master File

CONTRIBUTORS AND FUNDING SOURCES

Contributors

This work was supervised by a thesis committee consisting of Professors Gamal Akabani [adviser] and John Poston of the Department of Nuclear Engineering and Professor Victor Ugaz of the Department of Chemical Engineering.

All work for the thesis was completed by the student in collaboration with Dr. Gamal Akabani of the Department of Nuclear Engineering.

Funding Sources

This research was partially funded by the U.S. Department of Energy, Grant numbers DE-SC0007371 and DE-SC0008433, as well as the U.S. Nuclear Regulatory Commission, Grant number NRS 38 10 923

TABLE OF CONTENTS

Page

ABSTRACT ii

ACKNOWLEDGEMENTS iii

NOMENCLATURE iv

CONTRIBUTORS AND FUNDING SOURCES v

TABLE OF CONTENTS vi

LIST OF FIGURES viii

LIST OF TABLES ix

1. INTRODUCTION 1

1.1. Current world production and supply of ^{99}Mo 1
1.2. Current production using nuclear reactors 3
1.3. The coming shortage of ^{99}Mo 4
1.4. The directive of avoiding highly enriched uranium 5
1.5. Separation and purification of ^{99}Mo 6
1.6. Reactor and accelerator production of ^{99}Mo and ^{99m}Tc 8
1.7. Dedicated reactor based production 10
1.7.1. Fission of ^{235}U via ^{235}U(n,f)^{99}Mo 11
1.7.2. Activation of ^{98}Mo via ^{98}Mo(n,γ)^{99}Mo 13
1.8. Accelerator based production of ^{99}Mo and ^{99m}Tc 13
1.8.1. Accelerator induced fission of ^{235}U via ^{235}U(n,f)^{99}Mo 14
1.8.2. Photon-induced transmutation of ^{100}Mo via ^{100}Mo(γ,n)^{99}Mo 14
1.8.3. Direct production of ^{99m}Tc via ^{100}Mo(p,2n)^{99m}Tc 15
1.8.4. Photo-fission of ^{238}U via ^{238}U(γ,f)^{99}Mo 16
1.8.5. Production cost of new modalities 16
1.8.6. The issue of low specific activity 18
1.9. The need for regional diversified production and distribution of ^{99}Mo/^{99m}Tc 18
1.10. Proposed separation and concentration methods of ^{99}Mo/^{99m}Tc generators 19
1.10.1. Standard chemical separation method 20
1.11. U.S. Pharmacopeia and regulations 21
1.11.1. U.S. Pharmacopeia, USP <797> 22
1.12. Summary 23

2. MATERIALS AND METHODS 24

2.1. Physicochemical characteristics of natural molybdenum 24
2.2. Radiological properties of molybdenum radioisotopes 24
2.3. General equations for radionuclide production 26
2.4. Cross sections 28
2.5. Decay chains 28
2.6. Modeling the high-energy photon production 30
2.6.1. NIRTA Target System modification for bremsstrahlung production 30
2.6.2. Bremsstrahlung target modeling 33
2.6.3. Heat generation and dissipation 38
2.7. Health physics and hazards of high-energy electron accelerators 39
2.7.1. Photon and neutron production by high-energy photons 40
2.7.2. Hazards 41

3. RESULTS 45

3.1. Bremsstrahlung spectrum 45
3.2. Open channels, cross sections and reaction threshold energies 49
3.3. Irradiation products and reaction rates 49
3.4. Final products 57
3.5. Radiological safety 60
3.5.1. Neutron shielding 60
3.5.2. Bremsstrahlung shielding 61

4. DISCUSSION 63

4.1. Comparison between proposed and current production methods 63
4.2. Chemical separation of impurities 65

5. CONCLUSIONS 67

REFERENCES 68

APPENDIX A 73

APPENDIX B 80

LIST OF FIGURES

FIGURE		Page
1	Current global supply chain of ^{99}Mo generators, from uranium suppliers to users (NAS, 2016) ……..…….	3
2	Alternative production methods for ^{99}Mo and ^{99m}Tc (NAS, 2016)	9
3	Decay chain of ^{99}Mo ……..……..……..……..….	9
4	The thermal fission yield of ^{235}U (IAEA, 2006) ……...……..	12
5	Multicolumn Selectivity Inversion Generator (MSIG) strategy (Dash and Chakravarty, 2014) ……..…….	20
6	The NIRTA Solid Target System by IBA ……...	31
7	Molybdenum target disk holder used in the NIRTA solid target system …….…….	32
8	Collision, radiative and total electron stopping powers in tungsten (ESTAR) …….....	35
9	Cross sectional view with dimensions of tungsten target and molybdenum disk within the NIRTA target system ……...	36
10	Bremsstrahlung spectra for electron energies of 30, 35, 40 and 45 MeV ……	46
11	Bremsstrahlung spectra within the energy range of the cross section for ^{100}Mo(γ,n)^{99}Mo reaction ……..……..……..	47
12	Normalized fluence rate per LINAC electron energy as a function of LINAC electron energy ……..……..…….	48
13	Cross sections and neutron yields as a function of photon energy for the ^{nat}Mo(γ,x)n and ^{nat}W(γ,x)n ……..……..……...	62

LIST OF TABLES

TABLE		Page
1	The seven main nuclear reactors producing the world's supply of ^{99}Mo as of September 2016 ……	2
2	Comparison of current accelerator-driven options for ^{99}Mo production	17
3	Physicochemical properties of natural molybdenum …….	25
4	Radiological properties of stable and radioactive isotopes of molybdenum ……...	26
5	The performance parameters of the NIRTA target system ……	31
6	ESTAR data for stopping power, range, and fraction of bremsstrahlung production of electrons in a tungsten target …….	34
7	Noxious gases produced by radiation in air at electron LINACs ……..	43
8	Calculated reactions rates for ^{100}Mo based on ^{nat}Mo (mAs^{-1} cm^{-3}) …..	50
9	Calculated reactions rates for ^{98}Mo based on ^{nat}Mo (mAs^{-1} cm^{-3}) ……	51
10	Calculated reactions rates for ^{97}Mo based on ^{nat}Mo (mAs^{-1} cm^{-3}) ……	52
11	Calculated reactions rates for ^{96}Mo based on ^{nat}Mo (mAs^{-1} cm^{-3}) ……	53
12	Calculated reactions rates for ^{95}Mo based on ^{nat}Mo (mAs^{-1} cm^{-3}) ……	54
13	Calculated reactions rates for ^{94}Mo based on ^{nat}Mo (mAs^{-1} cm^{-3}) ……	55
14	Calculated reactions rates for ^{92}Mo based on ^{nat}Mo (mAs^{-1} cm^{-3}) ……	56
15	Calculated activities for radionuclides at end of bombardment (EOB) and end of cooling (EOC) per mA of LINAC electron beam current …	59

1. INTRODUCTION

1.1. Current world production and supply of ^{99}Mo

The metastable radionuclide ^{99m}Tc was first discovered in 1938 by Emilio Segré and Glenn T. Seaborg by bombarding natural molybdenum with 8 MeV deuterons using the cyclotron at the Ernest Orlando Lawrence's Radiation Laboratory (Seaborg and Segre, 1939; Segre and Seaborg, 1938). Afterwards, in 1940 Emilio Segré and Chien-Shiung Wu analyzed the fission products of ^{235}U and found the presence of ^{99}Mo and the corresponding ^{99m}Tc radionuclide (Segre and Wu, 1940). Three decades later, Eckelman and Richards developed the ^{99}Mo/^{99m}Tc generator and since then it is the preferred production and distribution method of method of ^{99m}Tc (Eckelman and Richards, 1970). Currently, there are seven nuclear reactors that produce the majority of ^{99}Mo needed for medical use (see Table 1). These nuclear reactors are more than 40 years old and require the use of highly enriched uranium (HEU) (Ballinger, 2010). After ^{99}Mo is produced in the nuclear reactors, it is sent to one of four major processing plants located in Canada, Belgium, The Netherlands, or South Africa (Cuttler, 2010) where only 5.8% of the fission yield of ^{235}U is ^{99}Mo with the rest being highly radioactive waste (IAEA, 2006).

The United States consumes between 5,000 and 7,000 Ci of the global 12,000 6-day Curie (activity produced after 6 days of irradiation) of Tc-99m per week. Unfortunately, there is no production site in the United States and all ^{99}Mo is imported from overseas (NRC, 2009). It is expected that the U.S. demand for ^{99}Mo will not rise

considerably over the next five years but international demand is expected to increase due to higher use in the Asian markets (NRC, 2009). The higher demand will cause a significant increase in the cost of the radionuclide across the world, but more exclusively, the US, if current methods of production are maintained. However, disruptions in production brought about by the shutdowns of the nuclear reactors due to their maintenance or decommissioning has already shown that production using nuclear reactors is unable to satisfy the current or future demand for ^{99}Mo.

Table 1
The seven main nuclear reactors producing the world's supply of ^{99}Mo as of September 2016 (Koster, 2013; NAS, 2016).

Reactor	Location	Country	Power (MW)	Reactor Fuel	Target	Operating since
NRU*	Chalk River	Canada	135	LEU	HEU	1957
HFR**	Petten	Netherlands	45	LEU	HEU	1961
BR2	Mol	Belgium	100	HEU	HEU	1961
LVR-15	Husinec	Czech Rep.	10	LEU	HEU	1989
SAFARI-1	Pelindaba	South Africa	20	LEU	HEU LEU	1965
OPAL	Lucas Heights	Australia	20	LEU	LEU	2007
Maria	Swierk	Poland	30	LEU	HEU	1974

** License expired in October 2016, but extended till March 2018*
*** Plans of shutdown since December 2010 but now awaiting substitution plant in 2024.(2014)*

1.2. Current production using nuclear reactors

The process of production of ^{99}Mo using nuclear reactors involves the fission of highly-enriched uranium (HEU) targets for a period of approximately one week. The targets are an alloy composed of aluminum and uranium (Cuttler, 2010). Irradiated targets are sent to a processing facility for the chemical separation of ^{99}Mo, capture and purification, generator assembly and final distribution to medical facilities. Fig. 1 presents the most current supply chain from uranium production, target preparation, reactor irradiation, ^{99}Mo separation, and distribution of ^{99}Mo generators (NAS, 2016).

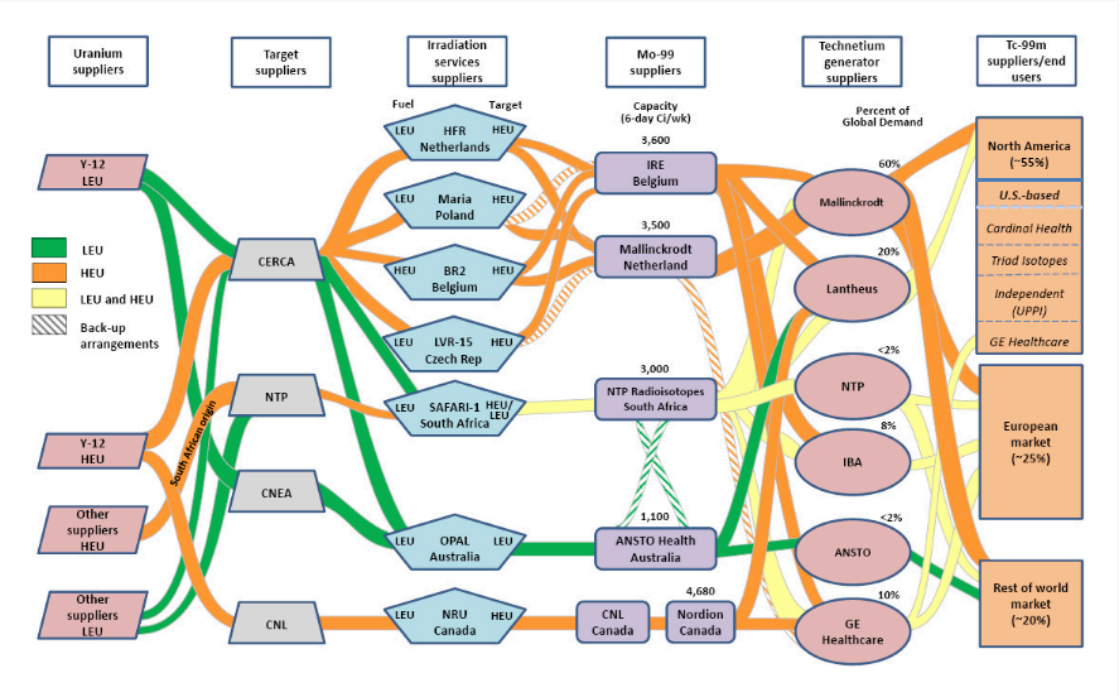

Fig. 1. Current global supply chain of ^{99}Mo generators, from uranium suppliers to users (NAS, 2016).

The nuclear reactor production process is arduous due to the involvement of HEU, the high costs associated with building and maintaining nuclear reactor facilities, and dealing with the disposal of hazardous nuclear waste. Furthermore, the supply of radionuclides produced in nuclear reactors is no longer a long-term and stable solution. Outages caused by routine and unforeseen maintenance have caused major disruptions in the supply of radionuclides for the nuclear medicine industry. These vulnerabilities have made the supply of medical radionuclides unreliable.

1.3. The coming shortage of ^{99}Mo

In 2009, the NRU research reactor in Canada, which was producing around 30% of the world's supply of ^{99}Mo at the time, was shutdown due to a heavy water leak (Cuttler, 2010). The interruption of production by such a major producer led to a shortage of the isotope, causing prices to rise and medical examinations to be cancelled. This event was the start of the ^{99}Mo shortage panic. Another shutdown of the NRU research reactor occurred in 2011 for regular maintenance. The NRU research reactor's license expired in October of 2016. However, the NRU research reactor's license has been extended until March of 2018 when the reactor will permanently shutdown and be decommissioned (Tollesfon, 2016). Additional nuclear reactors producing ^{99}Mo have been scheduled to permanently shutdown because of reaching their end-of-operational life and due to their high maintenance cost.

1.4. The directive of avoiding highly enriched uranium

In 2015 the U.S. Department of Energy's National Nuclear Security Administration started the Material Management and Minimization (M3) Conversion Program, which aims to reduce and subsequently eliminate the use of HEU in civil nuclear applications. The M3 conversion program is a continuation of the Global Threat Reduction Initiative established in 2004 to prevent the acquisition of nuclear and radiological materials for use in weapons of mass destruction and other acts of terrorism (Messick and Galan, 2013). Producers are trying to overcome the ^{99}Mo shortage and minimize the use of HEU by establishing alternative methods of production using low-enriched uranium (LEU). Research efforts are being made in the use of low-power or subcritical nuclear reactors utilizing aqueous fuel (IAEA). However, the use of aqueous fuel is still highly regulated and requires very costly and high maintenance nuclear reactor facilities.

The International Atomic Energy Agency has made significant efforts in establishing comprehensive programs among member nations to develop indigenous methods for the production of ^{99}Mo and ^{99m}Tc using low-enriched uranium (LEU) using research nuclear reactors and alternative production methods (IAEA, 2013). These efforts included the coordinated research projects (CRP) on Small Scale Indigenous ^{99}Mo Production, and accelerator-based alternatives to Non-HEU Production of ^{99}Mo/^{99m}Tc, which were conducted in Canada, Europe, and the U.S.A. and by the OECD/NEA.

1.5. Separation and purification of ^{99}Mo

Because of ^{99m}Tc has a short half-life of 6 hours; its parent nuclide ^{99}Mo ($T_{1/2}$ = 2.7 days) is provided to medical facilities in the form of a generator. Radionuclide generator design is mainly dependent on separation and adsorption science (Dash and Chakravarty, 2014). The rate of radionuclide uptake kinetics on a sorbent is measured in terms of the distribution or partition coefficient, K_d, which is defined as

$$K_d = \frac{\left(\frac{A_0 - A_S}{W}\right)}{\left(\frac{A_S}{V}\right)}, \qquad (1.1)$$

where A_0 and A_S are the aqueous phase activity before and after equilibration, respectively, commonly expressed in mCi or cpm units; W is the dry weight of the sorbent unit expressed in grams (g) and V is the volume of the aqueous phase (mL), expressed in units of mL/g. The partition coefficient K_d is a measure of the effectiveness of a solid phase to sorb a species from a solution. In general, if K_d values are >10,000, the sorbent effectively acts as a filter for the species of interest. If K_d values are between 10,000 and 1000, the separation is considered to be excellent. If K_d values are between 1000 and 100, the separation is good; and if the K_d values are between 100 and 10, the separation is poor. It is important to note that the adsorption of metal ions on inorganic supports is slow and may take several hours, and in some cases even days, to reach

equilibrium. Therefore, careful consideration is made on the type of sorbent, the physicochemical condition of the solution, and the deformation of the sorbent. The classical sorbent used in current HEU-based molybdenum generators is alumina (aluminum oxide, Al_2O_3). However, alumina is a poor sorbent in the presence of high concentration of uranium salt. Therefore, there is a need to develop new sorbents. Titanium oxide and Thermoxid sorbents have been developed and tested having much higher K_d values than alumina under many conditions, including uranium concentration and acidity.

A technical demonstration was carried out by a research group at the Los Alamos National Laboratory for the initial stage of ^{99}Mo recovery from a LEU sulfate solution in support of the commercialization of SHINE Medical Technologies production of ^{99}Mo using a Sachtopore® TiO_2 sorbent. These studies showed that less than 9% of ^{99}Mo remained in the uranium fraction post-contact. Furthermore, it was possible to recover more than 88% of the ^{99}Mo bound to the TiO_2 sorbent by using 0.1 mol L^{-1} of NaOH as the strip solution (May et al., 2013). These were encouraging results, which improved the reliability of LEU production of ^{99}Mo. A similar group at Argonne National Laboratory used Thermoxid sorbents for the separation and purification of ^{99}Mo and found it to be superior to alumina by a factor of 10 under high uranium concentration and various acidic levels. However, the K_d values for Mo capture for both Thermoxid and alumina sorbents were found to be inversely proportional to both the uranium salt concentration and acidity (Bakel et al., 2004).

1.6. Reactor and accelerator production of ^{99}Mo and ^{99m}Tc

Currently, the main production method of ^{99}Mo is by fission of ^{235}U in nuclear reactors, including future dedicated aqueous solution nuclear reactors. Alternative methods (Fig. 2) have either not achieved large-scale production or are under development (NAS, 2016). Nuclear reactors are the preferred production method for ^{99}Mo due to their unmatched production capabilities, including resulting high specific activity of ^{99}Mo. Whereas, accelerator production of ^{99}Mo, despite their lower production capacity, outperform reactor production methods with lower maintenance and construction costs, simpler licensing, safer operation and decommissioning, and minimal radioactive waste.

The decay scheme of ^{99}Mo is given in Fig. 3, it has a half-life $T_{1/2}$ = 65.9 h and decays into ^{99m}Tc (88%, $T_{1/2}$ = 6.01 h) and into ^{99g}Tc (12%, $T_{1/2}$ = 2.11×10^5 y), Ultimately, ^{99m}Tc decays to its ground state ^{99g}Tc, which in turn decays into ^{99}Ru following the emission of a beta particle (NRC, 2009).

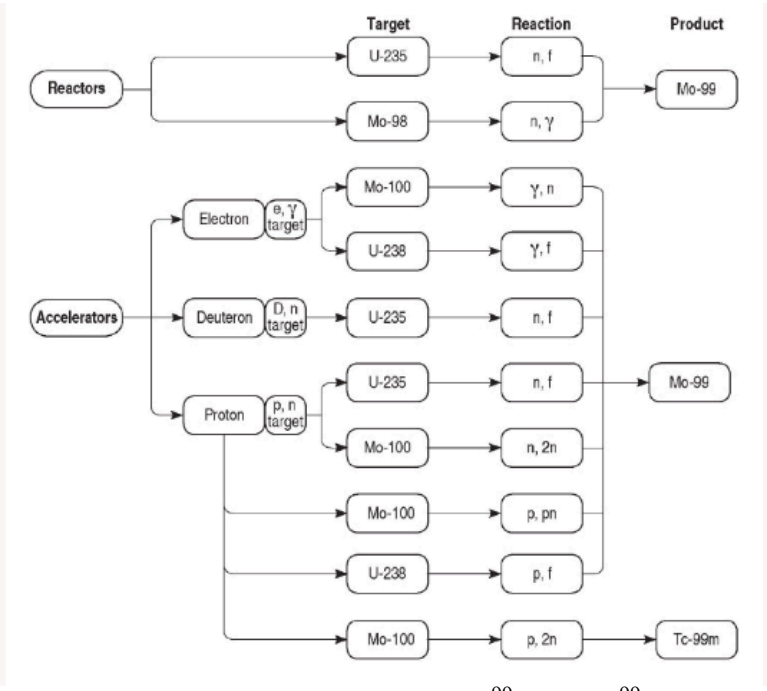

Fig. 2. Alternative proposed production methods for ^{99}Mo and ^{99m}Tc (NAS, 2016).

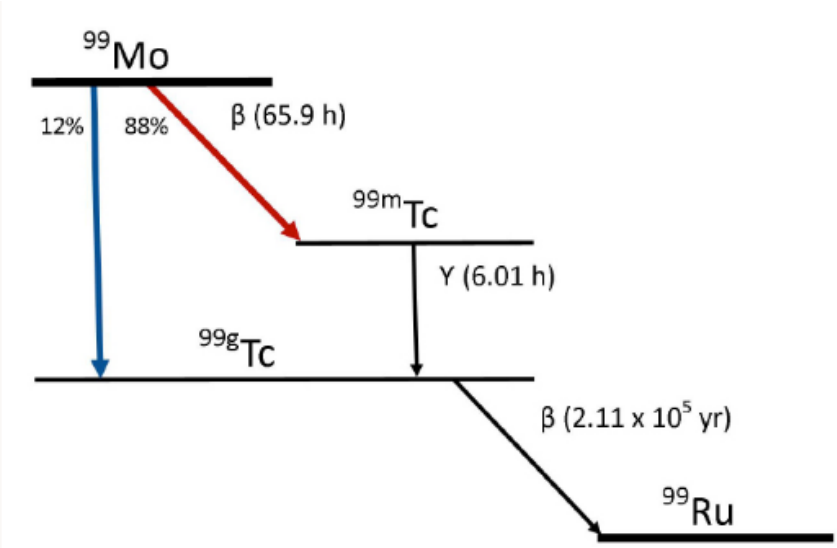

Fig. 3. Decay chain of ^{99}Mo.

1.7. Dedicated reactor based production

Nuclear reactors have been developed exclusively for the production of medical radionuclides. In 2005 the International Atomic Energy Agency (IAEA) established a Coordinated Research Project (CRP) studying the possibility of developing techniques for small-scale indigenous nuclear reactors for the production of ^{99}Mo by fission of LEU or by neutron activation of ^{98}Mo. This CRP was completed in 2011 and culminated with a publication in 2013 that summarized the work and accomplishments of the participants (IAEA, 2013). In 2009 the Organization for Economic Cooperation and Development (OECD) Nuclear Energy Agency (NEA) released a comprehensive report "The Supply of Medical Isotopes: An Economic Study of the Molybdenum-99 Supply Chain," which was the result of a comprehensive study carried out by the High-Level Group for Medical Radioisotopes (HEG-MR). The report compared in detail the production methods for ^{99}Mo. These studies have resulted in the establishment of dedicated nuclear reactors for the production of medical radionuclides in different countries.

Medical Isotope Production Reactors (MIPR) have been developed in China, the Russian Federation and the U.S.A. These are solution reactors based on LEU using liquid fuel, such as uranyl nitrate salt ($UO_2(NO_3)_2$) and uranyl sulphate (UO_2SO_4) salts as fuel. Four sorbents have been considered for molybdenum recovery. These are alumina, which is the classic inorganic sorbent for molybdenum recovery from acidic solutions, polyzirconium compound (PZC), developed in Japan to replace alumina in ^{99m}Tc generators for use in low specific activity ^{99}Mo generators, and two sorbents

specifically designed by Thermoxid in the Russian Federation for recovering ^{99}Mo from homogeneous reactor fuel solutions.

On the other hand, ^{99}Mo can be produced in low-fluence and high-fluence rate research reactors via neutron capture of ^{98}Mo. This method is being investigated in earnest by several countries, including Mexico, Argentina, and Chile. It is safe, it does not produce any significant radioactive waste or require costly separation facilities. The major impediment to its full implementation is the resulting low-specific activity of ^{99}Mo, which limits its applications in nuclear medicine procedures.

1.7.1. Fission of ^{235}U via ^{235}U(n,f)^{99}Mo

The irradiation of ^{235}U with thermal neutrons triggers its fission. The thermal neutron fission of ^{235}U produces a spectrum of fission products, including ^{99}Mo, ^{131}I, and ^{133}Xe. About 6.1 percent of the ^{235}U fissions produce ^{99}Mo, 6.3 percent produce ^{133}Xe, and 2 percent produce ^{131}I as shown in Fig. 4 (IAEA, 2006). The radionuclide ^{99}Mo is separated from the irradiated uranium target using an aqueous chemical process. Fission of ^{235}U has been the principal method of producing ^{99}Mo due to its high efficiency. The use of HEU results in a high specific activity usually, above 1000 curies per gram. The high specific activity of ^{99}Mo allows it to be used in conventional generators.

However, when salvaging ^{99}Mo from the irradiated uranium targets, large amounts of radioactive waste are produced. The waste produced includes uranium, and fission products, which must be placed in long-term storage facilities before disposal.

Processing off-gases such as the noble gases (^{131m}Xe, ^{133}Xe, ^{133m}Xe, and ^{135}Xe) and krypton (^{85}Kr) are also considered waste and must be stored for several months to allow for radioactive decay. Furthermore, the process liquids used during the uranium target dissolution are contaminated with fission and neutron activation products produced during irradiation.

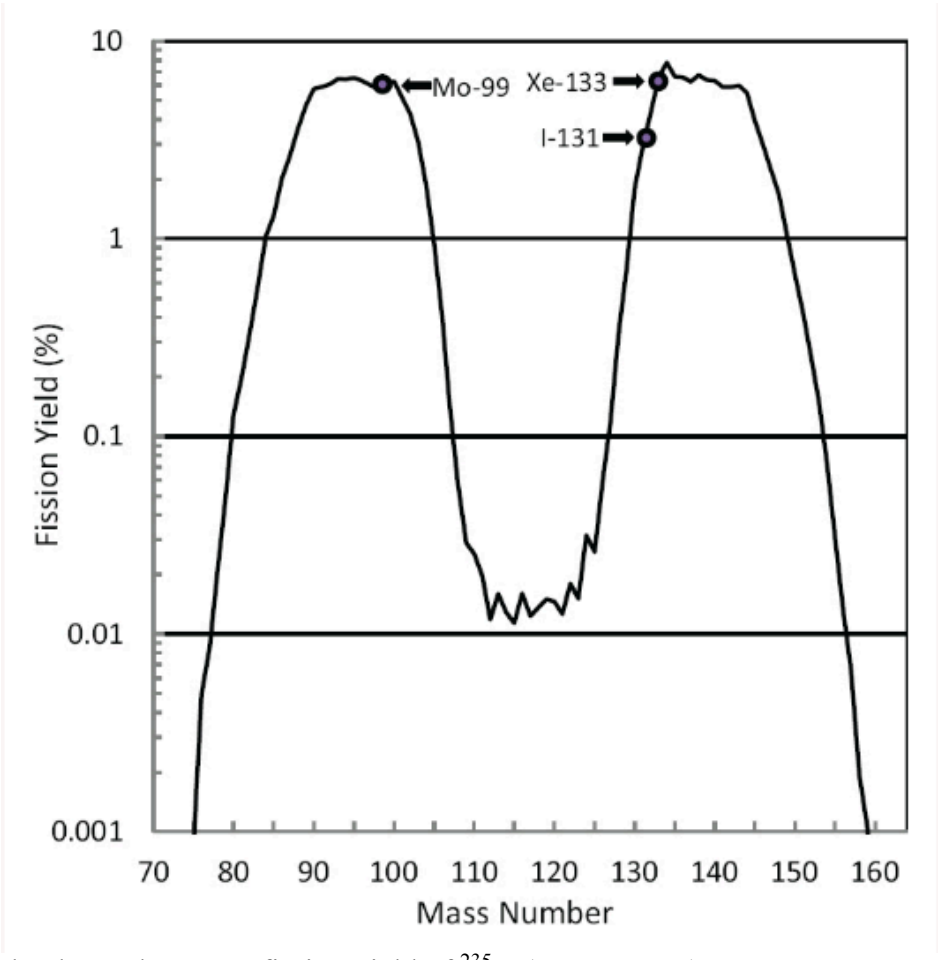

Fig. 4. The thermal neutron fission yield of ^{235}U (IAEA, 2006).

1.7.2. Activation of ^{98}Mo via ^{98}Mo(n,γ)^{99}Mo

The less preferred method of ^{99}Mo production in nuclear research reactors uses the neutron capture reaction with ^{98}Mo. The ^{98}Mo target is irradiated in the reactor with neutrons. Molybdenum-98 captures a thermal neutron and transmutes into ^{99}Mo following emission of a prompt gamma ray. This method is less preferred because neutron cross-section for ^{98}Mo (0.13 b) is over three orders of magnitude smaller than the fission cross section of ^{235}U (580 b) (IAEA, 1987). Furthermore, the ^{99}Mo produced has a very low-specific activity between 0.1 and 1 Curie per gram compared to 1000 Curies per gram when produced by fission of ^{235}U. The low-specific activity eliminates the possibility of using conventional ^{99m}Tc generators. Therefore, there is a need to develop new separation and concentration techniques that will allow increasing the final specific activity of ^{99m}Tc for clinical use (Dash and Chakravarty, 2014; Dash et al., 2012; Dash et al., 2013).

1.8. Accelerator based production of ^{99}Mo and ^{99m}Tc.

The use of particle accelerators for the production of ^{99}Mo and direct production of ^{99m}Tc has been studied extensively (Fig. 2). The use of a particle accelerator conveys certain advantages and disadvantages. Accelerators produce ion beams and accelerate ions to higher energies by using oscillating electromagnetic fields. The accelerated

particle beams have the capability of irradiating specific targets to produce ^{99}Mo and/or ^{99m}Tc.

1.8.1. Accelerator induced fission of ^{235}U via ^{235}U(n,f)^{99}Mo

Similar to the reactor-based production of ^{99}Mo by fission of ^{235}U, accelerators produce neutrons to trigger ^{235}U fission. Accelerators produce neutrons by accelerating protons or deuterons (proton-neutron pairs) into a high-Z material, such as tungsten. The resulting neutrons trigger ^{235}U fission and produce fission products identical to a reactor-based fission. However, accelerators produce neutron fluence rates that are one or two magnitudes lower than that of nuclear reactors. The low neutron fluence rate limits the subsequent ^{99}Mo production rate compared to reactor-based ^{99}Mo production.

1.8.2. Photon-induced transmutation of ^{100}Mo via ^{100}Mo(γ,n)^{99}Mo

Molybdenum-99 can be produced by separating neutrons from ^{100}Mo nuclei using high-energy bremsstrahlung photons (Danon et al., 2010). High-energy photons can be produced easily using high-energy electron accelerators (LINAC). This approach has numerous advantages over ^{99}Mo production using nuclear reactors. Advantages include safety and reduced production of radioactive waste. Operational cost, maintenance, and decommissioning costs are also drastically lower for LINACs (Starovoitova et al., 2014). Furthermore, electricity rather than fissile materials powers

these devices, thus producing less hazardous waste compared to the highly hazardous waste produced by nuclear reactors. LINACs also eliminate nuclear weapon proliferation risk and are not subjected to any NRC regulations pertaining to the use of uranium.

Achieving photonuclear reactions is now possible using high-energy LINACs. A converter made up of material with a high atomic number would be employed to produce high-energy bremsstrahlung photons in order to cause the photonuclear processes. A viable converter is a tungsten target (W) on which the high-energy electrons from the LINAC are incident and slowed down to emit bremsstrahlung photons.

A high-energy electron beam of approximately 40 MeV is sufficient for the production of bremsstrahlung photons. The final molybdenum target, on which the bremsstrahlung photons interact, is a ^{100}Mo target constructed in the form of nanoparticles glazed with a catcher material. (Starovoitova et al., 2014)

1.8.3. Direct production of ^{99m}Tc via ^{100}Mo(p,2n)^{99m}Tc

An initial feasibility study was carried out by Beaver and Hupf in 1971 to assess the direct production of ^{99m}Tc using a medical cyclotron via ^{100}Mo(p,2n)^{99m}Tc using 22 MeV protons. (Beaver and Hupf, 1971). With the advent of high-energy cyclotrons across many medical facilities this approach may become feasible. However, this strategy is limited to the production site with little capacity for distribution across multiple medical centers. Moreover, high-energy cyclotrons are expensive and require a large capital investment. The resulting ^{99m}Tc can be chemically separated using the

same principles of a generator and distributed to local radio pharmacies without any chemical processing or refining. However, pharmacies must be located near to the irradiation facility in order to receive ^{99m}Tc with sufficient specific activity.

1.8.4. Photo-fission of ^{238}U via ^{238}U(γ,f)^{99}Mo

Uranium-238 is a fertile nuclide and exists in nature with high abundance. Its fertility means that it is not capable of undergoing a fission reaction after absorbing thermal neutrons (Selek et al., 2015). Experimental cross section measurements of ^{238}U indicate that photon-induced fission is achievable easier than achieving neutron-induced fission of ^{238}U (Raj Prakash et al., 2011). Photo-fission of ^{238}U is induced by gamma rays produced via bremsstrahlung in a high-Z target (OECD, 2010).

1.8.5. Production cost of new modalities

The cost of producing ^{99}Mo using different methods is summarized in Table 2 (Bertsche, 2010). As indicated in the table, the most effective production method is that from accelerator-driven subcritical reactors (ADSR) using LEU. However, these costs do not take into consideration the costs of initial capital investment for infrastructure, maintenance, radioactive waste disposal, and decommissioning. However, when comparing the total cost, including capital investment, waste disposal, and

decommissioning, the overall cost of producing ^{99}Mo using a LINAC-based technique is comparable to an ADSR.

Table 2
Comparison of current accelerator-driven options for ^{99}Mo production (Bertsche, 2010; Nagai and Hatsukawa, 2009; Pramudita, 2011).

Accelerator type; Particle	Reaction	Energy	Beam Power	Target	6-day Ci/week	kWh/6-day-Ci
ADSR; Proton	^{235}U(n,f)^{99}Mo	1 GeV	1 MW	LEU	~6000	~25
ADSR; Proton	^{98}Mo(n,γ)^{99}Mo	1 GeV	1 MW	^{98}Mo	~3000	~50
ADSR; Proton	^{235}U(n,f)^{99}Mo	200 MeV	100 kW	LEU	~7000	~2.5
LINAC; Electron	^{238}U(n,f)^{99}Mo	50 MeV	1 MW	^{nat}U	~180	~900
LINAC; Electron	^{100}Mo(γ,n)^{99}Mo	>30 MeV	500 KW	^{100}Mo	~500	~170
LINAC; Electron	^{100}Mo(γ,n)^{99}Mo	25 MeV	20 KW	^{nat}Mo	~5	~800
Cyclotron; Proton	^{100}Mo(p,pn)^{99}Mo	45 MeV	4.5 KW	^{100}Mo	~2.5	~270
Cyclotron; Proton	^{100}Mo(p,pn)^{99}Mo	45 MeV	4.5 KW	^{nat}Mo	~0.25	~2700

ADSR: Accelerator driven subcritical reactor. LINAC: Linear accelerator.

1.8.6. The issue of low specific activity

Despite the advantage of relatively high yields in (γ,n) production, there exists the issue of low specific activity, or activity per unit mass. The low specific activity is due to the parent nuclide ^{100}Mo appearing with its daughter nuclide ^{99}Mo after irradiation (Starovoitova et al., 2014). To solve the issue of low specific activity, the parent and daughter nuclides must be separated and ^{99m}Tc re-concentrated to attain a high radionuclide concentration. Though it is not simple to separate two isotopes of the same chemical element, it is possible using the nuclear kinematic recoil. The main aim in solving the issue of low-specific activity would be to reduce the amount of the parent nuclide, ^{100}Mo, present in the final product of ^{99}Mo. Coating the ^{nat}Mo target particles with carbon, silicon carbide, or aluminum will serve as a barrier to reduce the amount of undesirable ^{100}Mo in the final product (Dash and Chakravarty, 2014).

1.9. The need for regional diversified production and distribution of ^{99}Mo/^{99m}Tc

As long as ^{99}Mo/^{99m}Tc maintains its status of being the most widely used radionuclide in nuclear medicine, a stable and regional supply solution will be required. Since the half-life of ^{99m}Tc (6 hours) is so short, not all nuclear medical facilities can rely on a few producers worldwide. To efficiently cater to all nuclear medicine facilities, accelerator radionuclide production centers must be established in areas corresponding to the high demands. The relatively low cost of setting up a radionuclide production

facility compared to nuclear reactors will interest entrepreneurs competing in the race of radionuclide production. Furthermore, accelerator radionuclide production facilities can be established without any geographical restrictions as defined by the USP 797 regulations (Atcher et al., 2016). The United States, for example, does not produce any ^{99m}Tc commercially and consumes half of the world's supply. A $6.5 billion market exists in the United States alone. A regional distribution network will facilitate the demands of major and minor nuclear medicine facilities' at a much lower cost.

1.10. Proposed separation and concentration methods of ^{99}Mo/^{99m}Tc generators

The proposed separation method for ^{99}Mo/^{99m}Tc involves a multicolumn selectivity inversion generator (MSIG) system shown in Fig. 5 (Dash et al., 2012). MSIG generators are alternatives to conventional radionuclide generator systems that use only one chromatographic column. The MISG concept involves preserving the daughter radionuclide ^{99m}Tc in a primary separation column while the parent radionuclide ^{99}Mo passes through the column. Afterwards, the daughter radionuclide is retrieved from the primary separation column and circulated through a secondary separation column called the guard column. The guard column traps any remaining parent radionuclides and allows the daughter radionuclide to escape free.

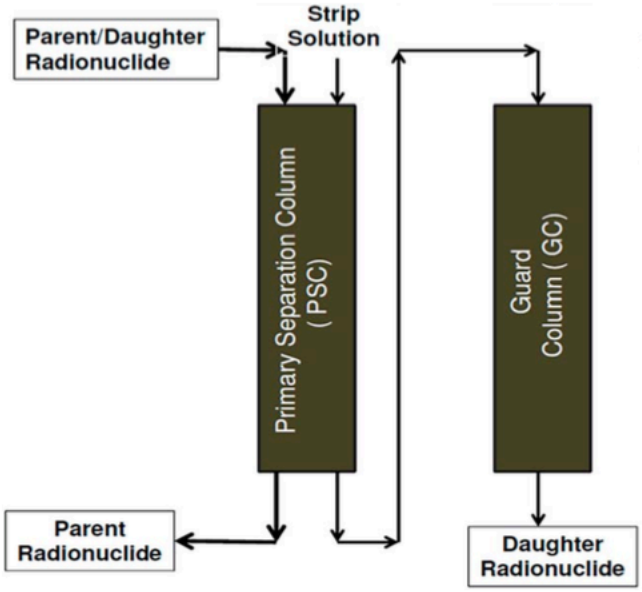

Fig. 5. Multicolumn Selectivity Inversion Generator (MSIG) strategy (Dash and Chakravarty, 2014).

1.10.1. Standard chemical separation method

Commercial $^{99}Mo/^{99m}Tc$ separation methods employ single column chromatography generators. The parent radionuclide ^{99}Mo is absorbed into alumina (Al_2O_3) in molybdate (MoO_4^{-2}) form. As the parent radionuclide ^{99}Mo decays, it forms pertechnetate (TcO_4^-), which is less strictly bound to the alumina (Dash and Chakravarty, 2014).

Finally, a normal saline solution is poured through the column containing the pertechnetate and immobilized ^{99}Mo to result in a final saline solution containing the ^{99m}Tc as the pertechnetate and sodium as the counterbalancing cation. The final sodium

pertechnetate solution can be used immediately at the medical facilities (Sarkar et al., 2013).

1.11. U.S. Pharmacopeia and regulations

Radionuclide, radiochemical, and chemical purities of the daughter radionuclide should be within the acceptable range prescribed in the pharmacopeias.

The USP regulation XXIII refers to the radionuclidic purity limits, "The United States Pharmacopeia (USP) XXIII specifies that technetium radiopharmaceuticals contain no more than 0.15 μCi of ^{99}Mo per mCi of ^{99m}Tc radiopharmaceutical at time of patient administration." The term "molybdenum breakthrough" describes ^{99}Mo being eluted along with the ^{99m}Tc during the separation process and must be minimized in order to comply with USP standards.

In reference to the chemical purity regulations, USP XXIII "allows no more than 10 micrograms of aluminum ion per milliliter of ^{99m}Tc eluate from a fission-produced generator." An excessive amount of aluminum is an indication of instability in the generator column allowing aluminum ions to be eluted along with the ^{99m}Tc.

With regards to radiochemical purity, the USP XXII has set minimum tagging efficiency standards where each pharmaceutical compound must be tested for radiochemical purity before use in a patient. Radiochemical impurity is created during the tagging process in radiopharmaceutical kits. In the tagging process, the ^{99m}Tc is tagged to a substrate molecule known as the ligand, which is designed to concentrate in a

specific organ system. The tagging process produces free sodium pertechnetate (^{99m}Tc) and hydrolyzed reduced ^{99m}Tc and they both give artifacts on the scanning. These artifacts may cause a misleading clinical diagnosis or difficulty in evaluating scans. Thus, ^{99m}Tc eluate must be tested for radiochemical purity before administering for diagnosis in patients. The ^{99m}Tc in the eluate must be detected and removed, as only the free sodium pertechnetate is needed. (Wilk, 2016)

1.11.1. U.S. Pharmacopeia, USP <797>

The U.S. Pharmacopeia Chapter 797 establishes the standards for both the radionuclides and non-radioactive medications handled, prepared, and stored in radiopharmacies of nuclear medicine departments. According to USP 797, the imaging agent ^{99m}Tc has a low microbial risk level (Atcher et al., 2016). Since ^{99m}Tc is classified as a low risk compounded sterile preparation (CSP), it is required to be prepared in a Class 5 environment described by the International Standards Organization (ISO). ISO Class 5 stipulates that the CSP must be performed in a specially designed, lead-lined, negative pressure, vertical airflow hood biological safety cabinet (BSC). These guidelines have been set forth to guarantee the safety of the CSP as well as shielding the operator from radiation exposure and radioactive contamination. Molybdenum-99/Technetium-99m generators with an ISO Class 5 BSC do not require the construction of a buffer and ante area thus reducing expenses.

USP also specifies that drugs must retain 90% to 100% of its potency in order to be used. Half-life decay times must be taken into account of CSP of $^{99}Mo/^{99m}Tc$ to comply with USP regulations with respect to administration of the radionuclide (Kastango and Weatherman, 2010).

1.12. Summary

This present research proposes a theoretical analysis for the regional production of $^{99}Mo/99$ using natural molybdenum via a photo-neutron reaction. This pivotal study is the first step in assessing an alternative method of production, which may result in a sustainable, long-term regional supply of ^{99}Mo without the need of reactors and use of HEU or LEU. The proposed method of production employs a (γ, n) reaction with natural molybdenum, and requires assessing the resulting specific activity of ^{99}Mo, and all potential radionuclidic impurities that may result during its production.

2. MATERIALS AND METHODS

2.1. Physicochemical characteristics of natural molybdenum

Molybdenum is a transition metal with an atomic mass of 95.94 (g mol^{-1}). In pure form, natural molybdenum is a silver-grey powder with a density of 10.3 g cm^{-3}, and melting and boiling points of 2,623 ^{o}C (4,753 ^{o}F) and 4,612 ^{o}C (8334 ^{o}F), respectively. Molybdenum is mainly used for the production of alloys with other metals such as steel due to its high melting point, strength and resistance to corrosion (Lepora, 2006). Table 3 provides a summary of its physiochemical properties. Sigma Aldrich supplies pure molybdenum powder with a purity of 99.99% (Sigma-Aldrich, 2017). The molybdenum powder can be pressed into a target disk holder made of aluminum using a cold isostatic pressing machine, which reduces the porosity and increases the density of molybdenum for irradiation purposes and structural integrity (ChinaTungsten, 2017).

2.2. Radiological properties of molybdenum radioisotopes

Molybdenum has seven stable isotopes and nine known radioisotopes. Table 4 presents the decay information as well as the abundance when applicable of the stable and radioactive isotopes of molybdenum.

Table 3
Physicochemical properties of natural molybdenum

Molecular weight	95.94 g mol^{-1}
Crystal Structure	Cubic Body Centered
Density	10.22 g cm^{-3}
Heat of Vaporization	6.431 kj g^{-1}
Heat of Fusion	0.391 kj g^{-1}
Specific Heat	251 J Kg^{-1} K^{-1}
Thermal Conductivity	138 W/m-K
Linear Expansion Coefficient	5.1000E-6/ K
Melting Point	2617 °C
Boiling Point	4612 °C
Atomic Radius	1.36 A
Covalent Radius	1.3 A
Susceptibility	89 microGauss
Resistivity	53.4 nanoOhm meter
Electron Affinity	0.746 eV
Electric Dipole Polariz	12.8 10-24 cc
Photoelectric Work	4.2 eV
Pauling Electronegativity	2.16
Oxidation State(s)	2 3 4 5 6
Ionization Potentials	7.099 V 16.15 V 27.16 V
Superconductivity	0.915 K
CAS Registry ID	7439-98-7
Bulk Modulus	230 GPa
Poisson Ratio	0.31
Shear Modulus	20 GPa
Young's Modulus	329 GPa

Table 4
Radiological properties of stable and radioactive isotopes of molybdenum.

Parent	Daughter	Decay Mode	Half-Life	Abundance
^{90}Mo	^{90}Nb	Positron	6.02 h	
^{91}Mo	^{91}Nb	Positron	15.49m	
^{92}Mo	^{92}Mo	Stable		15.7 %
^{93}Mo	^{93}Nb	Electron Capture	4000.11 y	
^{94}Mo	^{94}Mo	Stable		9.3 %
^{95}Mo	^{95}Mo	Stable		15.7 %
^{96}Mo	^{96}Mo	Stable		16.5 %
^{97}Mo	^{97}Mo	Stable		9.5 %
^{98}Mo	^{98}Mo	Stable		23.8 %
^{99}Mo	^{99}Tc	Beta	2.75 d	
^{100}Mo	^{100}Mo	Stable		9.5 %
^{101}Mo	^{101}Tc	Beta	14.61 m	
^{102}Mo	^{102}Tc	Beta	11.3 m	
^{103}Mo	^{103}Tc	Beta	1.167 m	
^{104}Mo	^{104}Tc	Beta	1.1 m	
^{105}Mo	^{105}Tc	Beta	5.0 m	

2.3. General equations for radionuclide production

For radionuclide production, activity and decay products are important aspects of the production cycle, which must be quantified. To ensure a final characterization of a target, stable and radioactive decay products must be analyzed based on estimated reaction rates, half-lives and decay chains to assess potential impurities that might remain in the final product. These impurities may require further processing before final clinical use. Impurities can also be avoided by lowering the accelerator electron beam

energy below specific reaction threshold energies. Impurities that are unavoidable must be removed by chemical separation using different sorbents.

The microscopic reaction rate is the basis for the production of various radionuclides during the irradiation of natural molybdenum. The microscopic reaction rate for a given open channel is given as

$$rr = \int s(E)\sigma(E)dE \tag{2.1}$$

where *s(E)* is the photon fluence rate with units of mA^{-1} cm^{-2} s^{-1} and $\sigma(E)$ is the microscopic cross section with units of cm^2 per atom. The photon fluence rate was calculated using Monte Carlo N-Particle code (MCNP) based on the geometry and material properties of the targets and the NIRTA solid target system.

The macroscopic reaction rate is used in the decay equations for every possible radionuclide produced during bombardment to assess the final activity levels for each radionuclide. The macroscopic reaction rate *RR*, is calculated as the product of the microscopic reaction rate *rr* and the atom density for the respective isotope N_i

$$RR = N_i \cdot rr \tag{2.2}$$

with

$$N_i = \frac{N_A \cdot \rho}{M} f_i \tag{2.3}$$

where N_A is Avogadro's number, M is the molecular weight (g mol^{-1}), ρ is the density (g cm^{-3}) and f_i is the natural abundance of isotope *i*.

2.4. Cross sections

The cross sections were obtained partly from experimental and evaluated nuclear reaction data compiled in the JANIS database by the Nuclear Energy Agency (Soppera et al., 2014). For absent experimental data, theoretical data from the nuclear data library TENDL 2015 were used (Koning and Rochman, 2012; Koning et al., 2015). The nuclear data in TENDL is obtained from the output of the TALYS nuclear model code system. The criteria for selection of cross sections were based on threshold energy of the open channels. Open channels were selected for analysis based on a normalized reaction rate to ^{100}Mo(γ,n)^{99}Mo higher than 1×10^{-8}. For radiation protection purposes, the cross sections for neutron production for natural molybdenum, ^{nat}Mo(γ,x)n, and natural tungsten, ^{nat}W(γ,x)n, were estimated using the computer code TALYS. All cross sections are expressed in units of mb (millibarn).

2.5. Decay chains

The decay chains for each radionuclide encountered in the production of ^{99}Mo were compiled and are presented in Appendix B. For a given decay chain, the physical decay constant for each involved radionuclide was used in conjunction with the

macroscopic reaction rate to calculate the final activity of the produced radionuclides at end of bombardment (EOB) and at the end of cooling (EOC) period. The differential equations describing the number of atoms per unit volume are as follows:

$$\begin{aligned}
\frac{dN_1}{dt} &= RR - \lambda_1 N_1 \\
\frac{dN_2}{dt} &= \lambda_1 N_1 - \lambda_2 N_2 \\
\frac{dN_3}{dt} &= \lambda_2 N_2 - \lambda_3 N_3 \\
&\vdots \\
\frac{dN_i}{dt} &= \lambda_{i-1} N_{i-1} - \lambda_i N_i
\end{aligned} \tag{2.4}$$

where the physical decay constant is defined as $\lambda_i = \ln(2)/T_{1/2,i}$, and N_i is the number of atoms per unit volume of target pertaining to radionuclide *i*. The open channels analyzed transform stable molybdenum isotopes into stable isotopes and radioisotopes, which further decay into other radionuclides. The decay equations are important for assessing the final atom and activity concentration levels for each potential impurity and for determining the methods of chemical separation needed to comply with USP and FDA regulations.

2.6. Modeling the high-energy photon production

The NIRTA targetry system was selected for the present pivotal study analysis. For bremsstrahlung photon production, a tungsten target, acting as a converter for high-energy electrons, was integrated into the NIRTA target system. The Monte Carlo transport code MCNP6 was used to model the production of high-energy bremsstrahlung (Goorley, 2012). The bremsstrahlung spectrum was normalized to the current being utilized in the LINAC and fluence rate was expressed in units of cm^{-2} mAs^{-1}. This normalization will help assess the needed total current to optimize the production cycle, and energy requirements.

2.6.1. NIRTA Target System modification for bremsstrahlung production

For the irradiation of molybdenum target disks, the NIRTA solid target system (Fig. 6) was chosen. The NIRTA solid target system is a compact solid target irradiation system, which can be easily installed on existing LINACs and cyclotrons for the production of non-conventional radionuclides. NIRTA solid target system is an industrial stand alone automated system supplied by Ion Beam Applications (IBA).

The solid target system is used for the stabilization and cooling of the molybdenum targets during irradiation. Cooling of the target is achieved by using chilled water to the rear and front face of the target. The performance parameters of the NIRTA solid target system are presented in Table 5.

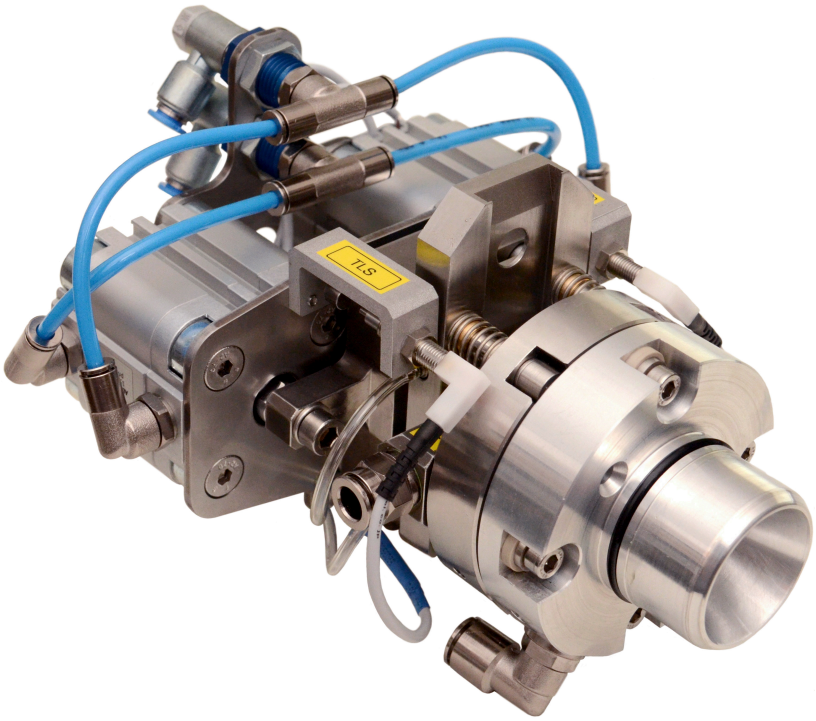

Fig. 6. The NIRTA Solid Target System by IBA.

Table 5
The performance parameters of the NIRTA target system.

Power and beam characteristics	
Maximum beam power	500 W
Minimum beam spot	8 mm FWHM
Target disk size	24 mm diameter / 2 mm thickness
Effective target spot	12 mm diameter
Cooling fluids consumption	
Front cooling	16 L per min of water
Back cooling	16 L per min of water
Coolant Pressure	0.5 MPa
Compressed Air	
Oil-free clean air	0.5 MPa
Operating conditions	
Temperature	+15 ^{o}C to +30 ^{o}C
Humidity	0 to 75 % RH

Modifications made to the existing NIRTA target system include the employment of a tungsten target. The tungsten target would be placed 0.87 cm before the molybdenum target along the electron beam line originating from the high-energy linear electron accelerator. The purpose of using a tungsten target is for the production of high-energy photons (bremsstrahlung) that would be incident on the molybdenum disk. The sudden stopping of high-energy electrons in a high-Z material target produces bremsstrahlung photons. Further information about the disk targets and the NIRTA target system is available in Appendix A. The tungsten target is shown in Fig. 7 where the grooves are used to increase the contact surface area of molybdenum during pressing. The total amount of molybdenum is measured by the weight difference of the target before and after pressing it. The outer and inner radii of the tungsten target disk were 12 and 6 mm, respectively. The thickness of the tungsten target disk and depth of the cavity were 2 and 1 mm, respectively

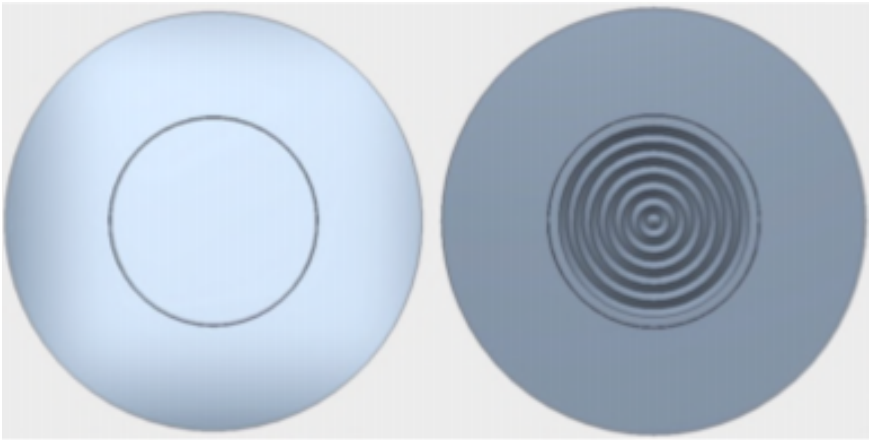

Fig. 7. Target disk holder made of aluminum used in the NIRTA solid target system.

2.6.2. Bremsstrahlung target modeling

The tungsten target was modeled as a cylinder with a diameter of 12.6 mm and thickness of 2.5 mm. These dimensions were based on maximizing high-energy bremsstrahlung production and heat dissipation while minimizing low energy bremsstrahlung production (below 9 MeV) by allowing high-energy electrons below 25 MeV to escape the tungsten target and deposit their energy into the water coolant. The distance between the tungsten and molybdenum targets was 0.87 cm based on the established geometry of the NIRTA targetry system.

The collision, radiative, total stopping powers, CSDA range, and radiation yield for electrons in tungsten were obtained using the code ESTAR (Fig. 8) from the National Institute for Standards and Technology (NIST) shown in Table 6. The electrons, and the fraction of kinetic energy of primary electrons converted into bremsstrahlung were obtained.

Table 6
ESTAR data for stopping power, range, and fraction of bremsstrahlung production of electrons in a tungsten target.

Kinetic Energy (MeV)	Collision Stopping Power (MeV cm^2/g)	Radiative Stopping Power (MeV cm^2/g)	Total Stopping Power (MeV cm^2/g)	CSDA Range (g/cm^2)	Radiation Yield
1.0	1.020	0.116	1.130	0.769	0.060
2.0	1.040	0.212	1.250	1.610	0.099
3.0	1.070	0.316	1.390	2.370	0.132
4.0	1.100	0.425	1.530	3.060	0.163
5.0	1.130	0.537	1.660	3.690	0.190
6.0	1.150	0.652	1.800	4.270	0.216
7.0	1.160	0.770	1.930	4.800	0.239
8.0	1.180	0.889	2.070	5.300	0.261
9.0	1.190	1.010	2.200	5.770	0.282
10.0	1.200	1.130	2.340	6.210	0.301
12.5	1.230	1.440	2.670	7.210	0.343
15.0	1.250	1.760	3.010	8.090	0.380
17.5	1.260	2.080	3.340	8.880	0.412
20.0	1.280	2.410	3.680	9.590	0.440
25.0	1.300	3.070	4.360	10.800	0.488
30.0	1.320	3.740	5.050	11.900	0.527
35.0	1.330	4.410	5.740	12.800	0.560
40.0	1.340	5.100	6.440	13.700	0.587

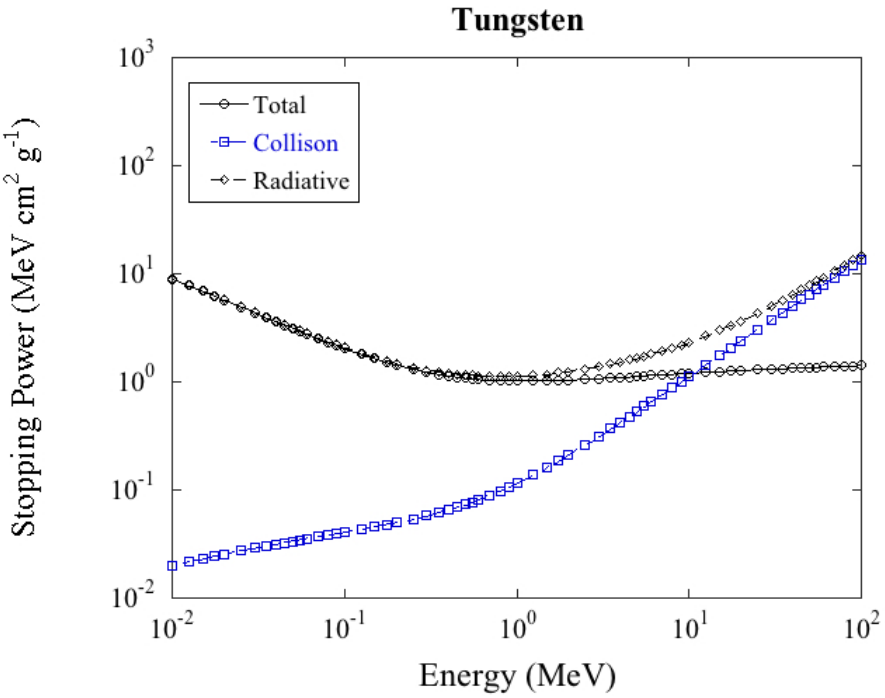

Fig. 8. Collision, radiative and total electron stopping powers in tungsten (ESTAR).

Bremsstrahlung production is forward peaked and increases with increasing energy. The angle at which the radiant energy is reduced by 50% is given as

$$\theta_{1/2} = \frac{100}{E_0} \ , \qquad (2.5)$$

where E_0 is the energy of the electron (Kosako et al., 2010; Nordell and Brahme, 1984; Takada et al., 2013). This equation denotes that below this critical angle, half of the radiant energy is concentrated between the angles between 0° and $\theta_{1/2}$. For 30, 35, 40, and 45 MeV electrons, $\theta_{1/2}$ = 3.3, 2.9, 2.5, and 2.2 degrees, respectively. This implies a very narrow distribution of the radiant energy, which requires the molybdenum disk to be as close as possible to the tungsten target thus maximizing the photon fluence. The cross sectional view of the tungsten target and molybdenum target placement within the NIRTA targetry system is shown in Fig. 9 along with the cooling lines for heat dissipation. The thicknesses of the tungsten target and molybdenum disk were 2.5 mm and 2 mm, respectively.

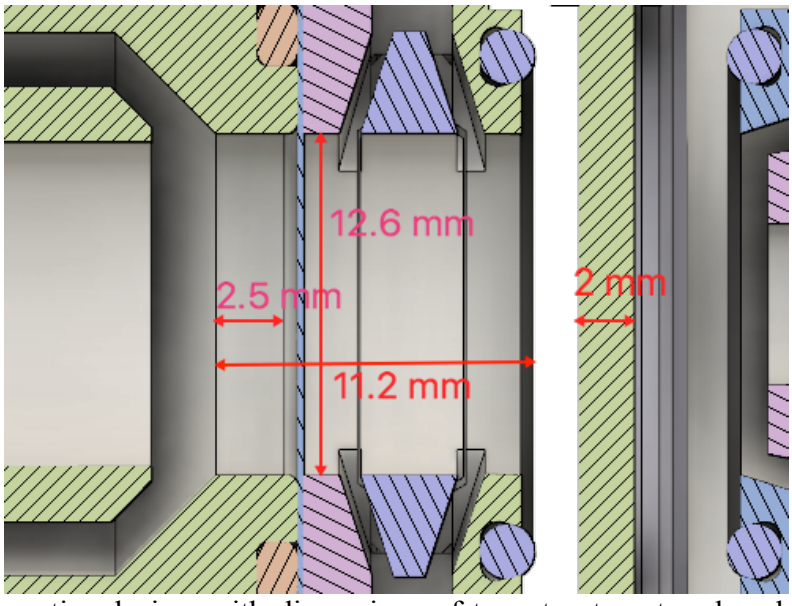

Fig. 9. Cross sectional view with dimensions of tungsten target and molybdenum disk within the NIRTA target system.

Bremsstrahlung production efficiency ε for thick targets is estimated as

$$\varepsilon = 1 - \frac{\ln\left(1 + 1.2 \times 10^{-3} TZ\right)}{1.2 \times 10^{-3} TZ}, \tag{2.6}$$

where T is kinetic energy of the electron and Z is the atomic number of the target material (NCRP, 1964). For electrons with energies of 40 MeV and a tungsten target (Z = 74), the resulting efficiency ε is 0.57, which confirms ESTAR's data approximation of 0.587 for the fraction of bremsstrahlung production at 40 MeV. Moreover, the forward bremsstrahlung intensity produced by high-energy LINACs is given as

$$I(O) = 0.72 \times 10^{-4} \left(T + m_0 c^2\right) TK \ln\left(\frac{950t}{t_r}\right), \tag{2.7}$$

expressed in units of $\left(\text{Watts}/\text{cm}^2\text{-mA}\right)$ at 1 meter, where t is the target thickness in cm, and t_r is the radiation length, which for tungsten is 6.76 g/cm^2, and K is equal to 0.888 (NCRP, 1964). As an example, for a 40 MeV LINAC with a tungsten target with thickness of 0.25 cm, the forward power intensity from bremsstrahlung will be 0.36 $\left(\text{Watts}/\text{cm}^2\text{-mA}\right)$. This will be concentrated within a solid angle subtended by $\theta_{1/2}$ as previously described in Eq. (2.5).

2.6.2.1. Optimal bremsstrahlung energy spectrum

The Monte Carlo transport code MCNP was used to calculate the bremsstrahlung spectrum. The fluence rate was calculated over the target of molybdenum of thickness 0.2 cm. The bremsstrahlung photons produced in the tungsten target incident to the molybdenum target were tallied to assess the bremsstrahlung spectrum. The optimal spectrum was analyzed for LINAC electron energies between 35 and 45 MeV to establish the electron energy at which the photon fluence rate was maximum at 14 MeV while minimizing undesirable reactions and power consumption.

2.6.3. Heat generation and dissipation

Heat dissipation generated in the components of the LINAC and NIRTA targetry system are important to maintain target integrity and optimal operation of the accelerator. The total power generated by the LINAC electron beam is given by

$$P = I \cdot V \ , \tag{2.8}$$

where I is the electron current generated by the LINAC expressed in units of amperes, and V is the voltage measured in electron volts. Heat dissipation will be required for the tungsten target, the molybdenum disk, and component of the NIRTA targetry system. The fraction of power deposited in the tungsten target will be $(1-\varepsilon)$, requiring

significant cooling at the back of the target. For the 40-MeV electron beam with a current of 2 mA, the total power generated by the beam was 80 kW where 34.4 kW was deposited in the thick tungsten target and 45.6 kW was dispersed in the form of bremsstrahlung.

2.7. Health physics and hazards of high-energy electron accelerators

The operation of a high-energy LINAC carries significant hazards. The primary hazard encountered is activation of shielding and accelerator components. Choosing low activation materials placed in well exposed areas and shielding of the entire area are of great importance when designing an high-energy accelerator facility (NCRP, 1964). Secondary hazards include heat generation, concentration and dispersion of noxious gases, electrical hazards and fire. These hazards can be mitigated by abiding to safety protocols and recommendations (NCRP, 2005).

High-energy accelerators produce radiation fields of high energy and intensity composed of photons and neutrons. Protecting against such high intensity radiation fields require the attenuation of the radiation to acceptable levels using adequate thicknesses and materials of shielding materials. The extent to which radiation must be reduced depends on the radiation source, distance between the source and dose area of interest, time that workers or the public spend in the radiation area, and the necessary dose limits outside the shielded area.

For high-energy electron accelerators, the main focus of shielding is on the diverse prompt radiation fields resulting from the interaction of high-energy electrons with matter and targets.

To effectively derive shielding specifications, 1) the physical lay-out of the facility must be assessed, 2) dividing the facility area to determine shielding zones, 3) defining primary and secondary radiations possible during normal, special, and emergency operation situations, 4) defining maximum dose rates for areas exterior to the facility, 5) calculating the attenuation needed for all sources and areas, 6) estimating shielding materials and thickness required for adequate attenuation, 7) designing a preliminary shielding layout, 8) evaluating total attenuation by shielding layout and identify any conflicts, 9) redesigning and implementing a final layout.

2.7.1. Photon and neutron production by high-energy photons

High-energy photons, usually above 15 MeV, produce neutrons through photonuclear interactions. Neutrons will be generated by photons being produced inside the tungsten target and impacting the molybdenum disk. The total neutron cross sections for tungsten, $^{nat}W(\gamma,x)n$, and molybdenum, $^{nat}Mo(\gamma,x)n$, and corresponding neutron yields as a function of incident photon energy were estimated using the computer code TALYS (Koning and Rochman, 2012). The resulting cross sections and yields were used to assess the total neutron fluence rate (s^{-1}) and neutron energy spectrum generated by the accelerator.

To attenuate neutrons of energies greater than 20 MeV, the optimal shielding design should involve the use of advanced boron-based shielding materials for neutrons and high-energy photons (Hayashi et al., 2009; Yilmaz et al., 2011).

2.7.2. Hazards

Hazards at a high-energy electron accelerator must be addressed as they might have adverse effects on personnel operating the accelerator and hinder successful operation. Good design and construction of high-energy electron accelerators with subsequent routine safety procedures at accelerator facilities will ensure radiological safety during operation and after shutdown.

Irradiated material may be considered a fire hazard due to the deposition of significant energy. Also, radiation catalysis of exothermic chemical reactions makes irradiated materials a fire hazard. Furthermore, chemical vapors from irradiated volatile inorganic materials maybe produce an explosive mixture. The methods used to avoid fire hazards include using air circulation and retardants.

2.7.2.1. Electrical hazards

Accelerators are specifically vulnerable to electrical hazards due to the high electrical currents used to generate high-energy electrons. Accelerators are also susceptible to further electrical hazards caused from nuclear radiation effects. Such hazards could include high voltage charges accumulating on leaded glass windows and target materials and systems during operation. All special-purpose particle accelerator need to comply with the National Electric Code® and the National Fire Protection Association (NFPA), "Standard for Electrical Safety in the Workplace," which include the electrical safety practices established in 29 CFR 1910 Subpart S, 29 CFR 1910.269, control of hazardous energy 29 CFR 1910.147, and fire protection as indicated for means of egress, 29 CFR 1910.33-39, and subpart L, and fire protection, 29 CFR 1910.155-165.

2.7.2.2. Noxious gas production

Noxious gases are produced by ionizing radiation via reactions of high-energy electrons in air. One molecule of noxious gas is produced per ion pair in air, the average energy required to produce an ion pair in air is 33.7 eV. The total number of noxious gasses produced per second (dM/dt) by a beam current of I mA, travelling through a distance t cm in air can be calculation using Eq. 2.9.

$$\frac{dM}{dt} = \frac{2.2 \times 10^3}{33} 6.25 \times 10^{15} \cdot I \cdot t \,, \qquad (2.9)$$

where I is the beam current measured in mA, t is the thickness of air measured in centimeters, M is the mass of noxious gases, and 1 mA is 6.25×10^{15} electrons per second (NCRP, 1964). This equation is a conservative estimate as more than half of the energy will be dissipated in the tungsten target and the rest converted into bremsstrahlung.

The main noxious gases produced at an electron LINAC facility are presented in Table 7. Ozone gas (O_3) is the most toxic gas produced in significant quantities that might cause a health hazard. The highest concentration of toxic gases would be in the area where the highest radiation doses to air occur; this will correspond to the forward bremsstrahlung intensity.

Table 7
Noxious gases produced by radiation in air at electron LINACs

Gas	Notation	Threshold limit value (ppm)
Ozone	O_3	0.1
Nitric oxide	NO	25
Nitrogen Dioxide	NO_2	5*

*Maximum concentration allowed at any time

However, ozone gas decomposes naturally through reactions with air impurities and decomposes by radiation itself. Average decomposition time for a standard research laboratory is around 50 minutes depending on the room size, temperature, impurities in

air and respective charges, wall material, and ozone concentration. In order to mitigate the effects of toxic gases, the electron beam path-length may be minimized to reduce the integral dose deposited in air. This is accomplished by increasing the ventilation rate and prohibiting personnel entry during and after irradiation.

3. RESULTS

3.1. Bremsstrahlung spectrum

The bremsstrahlung spectrum generated by the high-energy LINAC was calculated using the Monte Carlo code MCNP based on the geometry and material properties of the NIRTA target system. The spatial distribution of the electrons impacting the tungsten target was modeled using a truncated normal distribution. The fluence rate was calculated using an F4 tally card over the molybdenum target. Monte Carlo calculations of the bremsstrahlung spectrum were carried out at 30, 35, 40 and 45 MeV LINAC electron energies and normalized to the electron current of the LINAC. (Fig. 10).

The LINAC electron energy is optimized at a photon energy of 14 MeV, where the cross section for the ^{100}Mo(γ,n)^{99}Mo reaction is maximum. The optimization was accomplished by maximizing the fluence rate of the bremsstrahlung spectrum at 14 MeV per unit energy of the LINAC. Therefore, the optimization function is given as

$$\max\left(\frac{\varphi(14\ \text{MeV})}{E_{LINAC}}\right) \tag{3.1}$$

where E_{LINAC} is the electron energy of the accelerator and $\varphi(14\ \text{MeV})$ is the bremsstrahlung fluence rate at 14 MeV. The resulting bremsstrahlung spectra for LINAC

electron energies of 30, 35, 40 and 45 MeV and the cross sections for $^{100}Mo(\gamma,n)^{99}Mo$ reaction are shown in Fig. 11 describing an increase in fluence rate as a function of LINAC electron energy. Fig. 12 shows the resulting normalized fluence rate at 14 MeV per unit energy as a function of LINAC electron energy. Based on these data, the resulting optimal energy was estimated at 40 MeV.

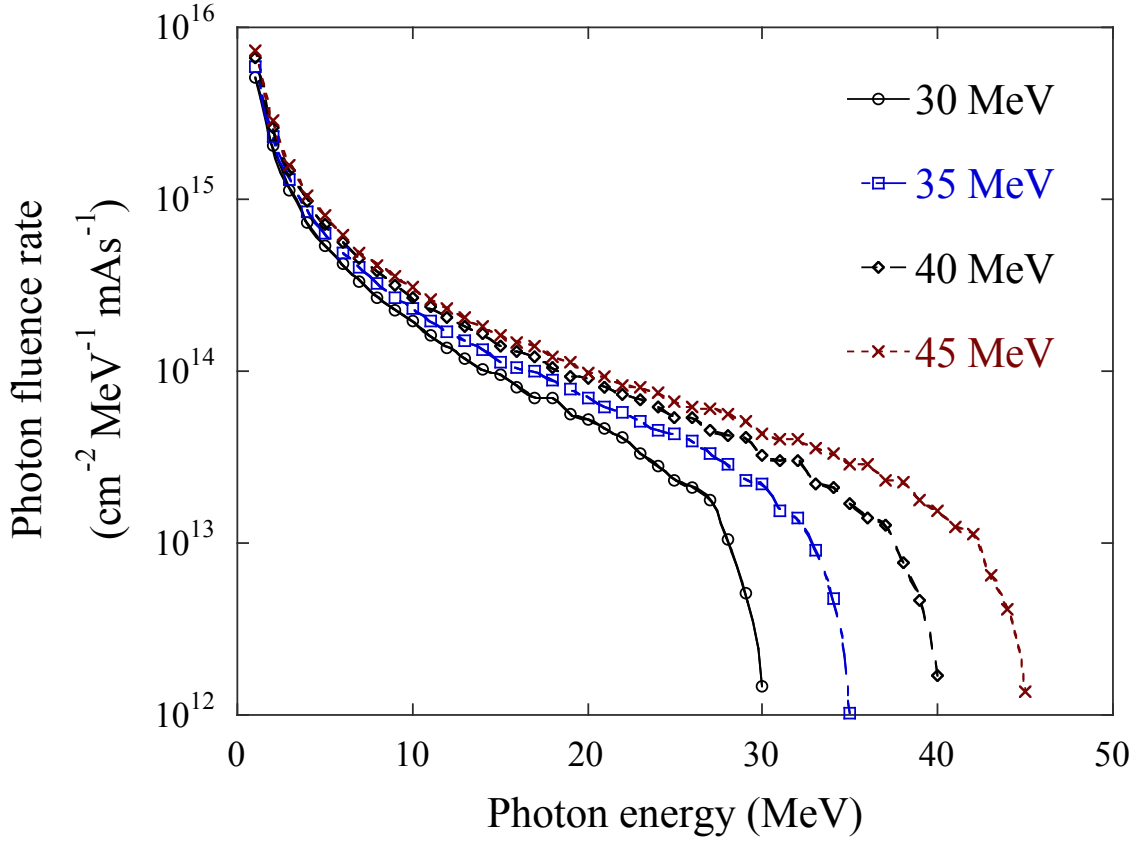

Fig. 10. Resulting bremsstrahlung spectra for electron energies of 30, 35, 40 and 45 MeV.

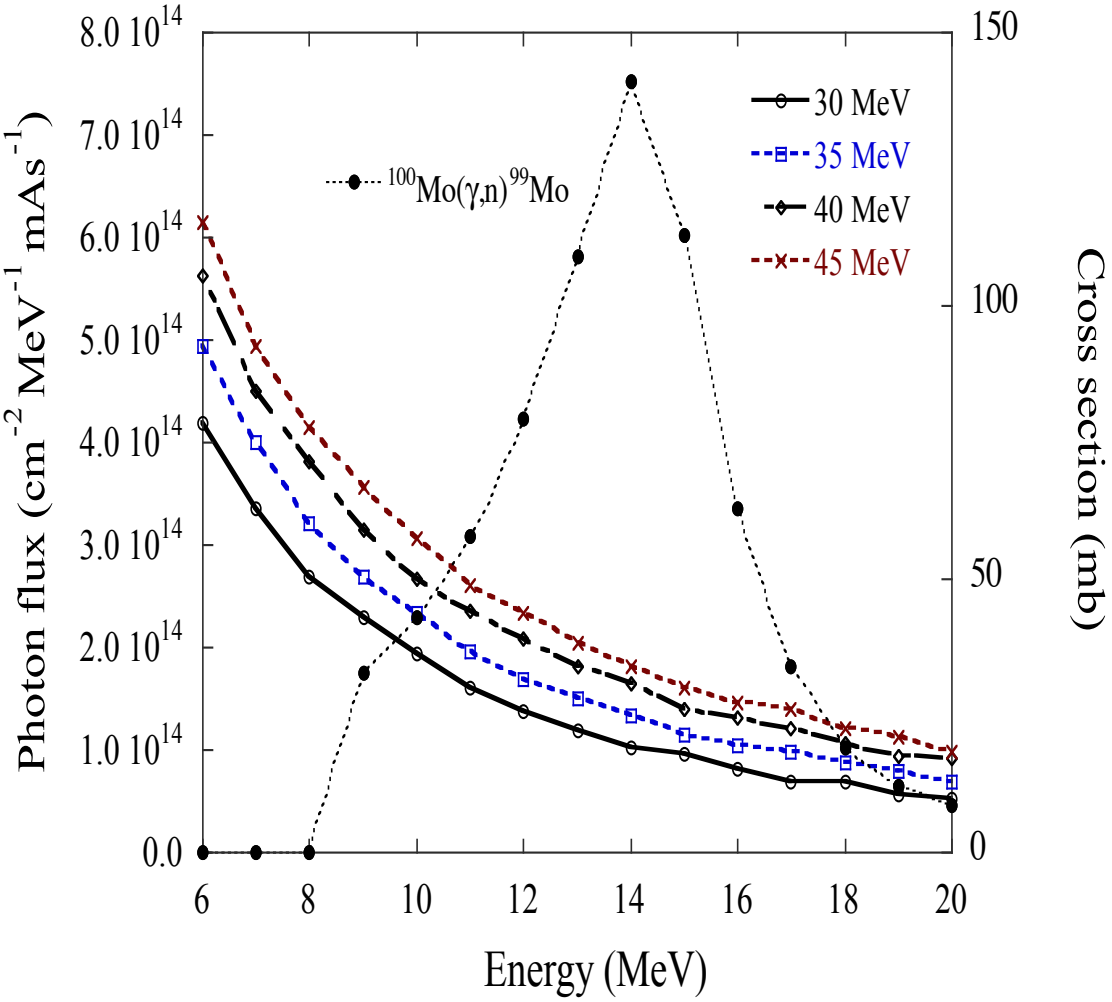

Fig. 11. Bremsstrahlung spectra within the energy range of the cross section for $^{100}Mo(\gamma,n)^{99}Mo$ reaction.

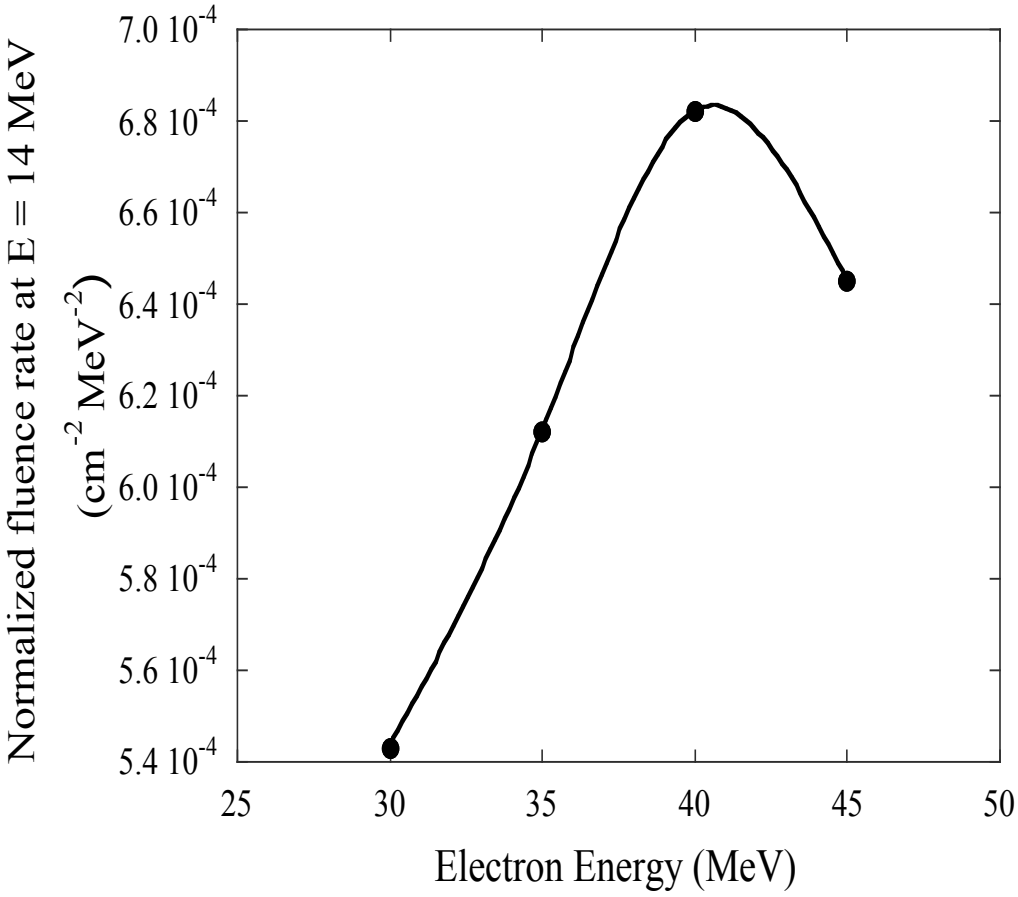

Fig. 12. Normalized fluence rate per LINAC electron energy as a function of LINAC electron energy.

3.2. Open channels, cross sections and reaction threshold energies

Open channels are the possible reactions encountered during operation. All open channels with molybdenum isotopes were considered by taking into account their reaction Q-values and corresponding threshold energy. The Q-values and threshold energies were obtained from the National Nuclear Data Center, Atomic Mass Data Center, Q-value calculator (NNDC, 2017). These Q-values and threshold energies were further corroborated using the TENDL database or the TALYS computer code (Koning et al., 2015). The following open channels were considered: (γ,n), (γ,2n), (γ,3n), (γ,p), (γ,2p), (γ,3p), (γ,n+p), (γ,2n+p), (γ,3n+p), (γ,d), (γ,t), (γ,^{3}He), and (γ,a). The resulting reaction products can be in metastable or ground state energy. Therefore, it was important to consider the radionuclides that have long-lived metastable states, which may remain in the final product.

3.3. Irradiation products and reaction rates

The macroscopic reaction rate for each open channel was calculated using the 40-MeV bremsstrahlung spectrum. Tables 8 through 14 summarize the results for ^{100}Mo, ^{98}Mo, ^{97}Mo, ^{96}Mo, ^{95}Mo, ^{94}Mo, and ^{92}Mo, respectively, showing the reaction open channels, estimated reaction rates (mAs^{-1} cm^{-3}), the normalized reaction rates to ^{100}Mo(γ,n)^{99}Mo, and the half-life of each of the reaction products. The reaction rate for each given product was then used in their respective decay equations to estimate the

final atom concentration and activity (yield) in the molybdenum target at the end of bombardment (EOB), and end of cooling (EOC) at 1 and 2 hours post bombardment.

Table 8
Calculated reactions rates for ^{100}Mo based on ^{nat}Mo (mAs^{-1} cm^{-3}).

	Reaction	Reaction rate	Normalized reaction rate†	Half-life
1	^{100}Mo(g,n)^{99}Mo	7.86E+11	1.00E+00	2.7 d
2	^{100}Mo (g,2n)^{98}Mo	5.22E+11	6.64E-01	Stable
3	^{100}Mo (g,3n)^{97}Mo	3.68E+10	4.69E-02	Stable
4	^{100}Mo (g,p)^{99}Nb	1.04E+09	1.32E-03	15 s
5	^{100}Mo (g,2p)^{89}Zr	2.26E+04	2.88E-08	3.27 d
6	^{100}Mo (g,n+p)^{98m}Nb	2.03E+08	2.59E-04	51.3 m
7	^{100}Mo (g,n+p)^{98}Nb	5.51E+08	7.01E-04	2.86 s
8	^{100}Mo (g,2n+p)^{97}Nb	1.57E+08	1.99E-04	1.2 h
9	^{100}Mo (g,n+2p)^{97}Zr	6.00E+03	7.64E-09	16.9 h
10	^{100}Mo (g,d)^{98m}Nb	2.57E+07	3.27E-05	51.3 m
11	^{100}Mo (g,d)^{98}Nb	8.59E+07	1.09E-04	2.86 s
12	^{100}Mo (g,t)^{97m}Nb	8.76E+05	1.11E-06	58.7 s
13	^{100}Mo (g,t)^{97}Nb	2.08E+06	2.65E-06	1.2 h
14	^{100}Mo (g,^{3}He)^{97}Zr	7.32E+03	9.32E-09	16.9 h
15	^{100}Mo(g,a)^{96}Zr	5.31E+07	6.76E-05	Stable

† Normalized reactions rates to ^{100}Mo(g,n)^{99}Mo reaction

Table 9
Calculated reactions rates for ^{98}Mo based on ^{nat}Mo (mAs^{-1} cm^{-3}).

	Reaction	Reaction rate	Normalized reaction rate†	Half-life
1	^{98}Mo(g,n)^{97}Mo	2.18E+12	2.77E+00	Stable
2	^{98}Mo(g,2n)^{96}Mo	7.84E+11	9.97E-01	Stable
3	^{98}Mo(g,3n)^{95}Mo	4.20E+10	5.34E-02	Stable
4	^{98}Mo(g,p)^{97m}Nb	2.02E+09	2.58E-03	58.7 s
5	^{98}Mo(g,p)^{97}Nb	2.03E+09	2.58E-03	1.2 h
6	^{98}Mo(g,2p)^{96}Zr	2.69E+05	3.42E-07	Stable
7	^{98}Mo(g,n+p)^{96}Nb	2.48E+09	3.15E-03	23.35 h
8	^{98}Mo(g,2n+p)^{95m}Nb	1.37E+08	1.74E-04	3.61 d
9	^{98}Mo(g,2n+p)^{95}Nb	4.66E+08	5.93E-04	34.991 d
10	^{98}Mo(g,3n+p)^{94m}Nb	7.73E+06	9.83E-06	6.26 m
11	^{98}Mo(g,3n+p)^{94}Nb	1.42E+06	1.80E-06	2.03E+4 y
12	^{98}Mo(g,n+2p)^{95}Zr	1.18E+05	1.49E-07	63.032 d
13	^{98}Mo(g,d)^{96}Nb	2.48E+08	3.16E-04	23.35 h
14	^{98}Mo(g,t)^{95m}Nb	1.05E+06	1.33E-06	3.61 d
15	^{98}Mo(g,t)^{95}Nb	2.67E+06	3.39E-06	34.991 d
16	^{98}Mo(g,^{3}He)^{95}Zr	2.48E+04	3.15E-08	63.032 d
17	^{98}Mo(g,a)^{94}Zr	6.23E+08	7.92E-04	Stable

† Normalized reactions rates to ^{100}Mo(g,n)^{99}Mo reaction

Table 10
Calculated reactions rates for ^{97}Mo based on ^{nat}Mo (mAs^{-1} cm^{-3}).

	Reaction	Reaction rate	Normalized reaction rate†	Half-life
1	^{97}Mo(g,n)^{96}Mo	8.29E+11	1.05E+00	Stable
2	^{97}Mo(g,2n)^{95}Mo	3.04E+11	3.86E-01	Stable
3	^{97}Mo(g,3n)^{94}Mo	1.77E+10	2.26E-02	Stable
4	^{97}Mo(g,p)^{96}Nb	3.55E+09	4.51E-03	23.35 h
5	^{97}Mo(g,2p)^{95}Zr	2.89E+05	3.68E-07	63.032 d
6	^{97}Mo(g,n+p)^{95m}Nb	3.82E+08	4.86E-04	3.61 d
7	^{97}Mo(g,n+p)^{95}Nb	1.85E+09	2.35E-03	34.991 d
8	^{97}Mo(g,2n+p)^{94m}Nb	2.71E+08	3.45E-04	6.26 m
9	^{97}Mo(g,2n+p)^{94}Nb	1.02E+08	1.29E-04	2.03E+4 y
10	^{97}Mo(g,n+2p)^{94}Zr	2.11E+05	2.69E-07	Stable
11	^{97}Mo(g,d)^{95m}Nb	2.45E+07	3.11E-05	3.61 d
12	^{97}Mo(g,d)^{95}Nb	1.18E+08	1.50E-04	34.991 d
13	^{97}Mo(g,t)^{94m}Nb	1.38E+06	1.75E-06	6.26 m
14	^{97}Mo(g,t)^{94}Nb	3.67E+05	4.67E-07	2.03E+4 y
15	^{97}Mo(g,^{3}He)^{94}Zr	2.55E+04	3.24E-08	Stable
16	^{97}Mo(g,a)^{93}Zr	6.90E+08	8.78E-04	1.61E+6 y

† Normalized reactions rates to ^{100}Mo(g,n)^{99}Mo reaction

Table 11
Calculated reactions rates for ^{96}Mo based on ^{nat}Mo (mAs^{-1} cm^{-3}).

	Reaction	Reaction rate	Normalized reaction rate†	Half-life
1	^{96}Mo(g,n)^{95}Mo	1.49E+12	1.89E+00	Stable
2	^{96}Mo(g,2n)^{94}Mo	4.15E+11	5.27E-01	Stable
3	^{96}Mo(g,3n)^{93m}Mo	3.04E+07	3.87E-05	6.85 h
4	^{96}Mo(g,3n)^{93}Mo	1.83E+10	2.33E-02	4.0E+3 y
5	^{96}Mo(g,p)^{95m}Nb	2.28E+09	2.90E-03	3.61 d
6	^{96}Mo(g,p)^{95}Nb	4.57E+09	5.81E-03	34.991 d
7	^{96}Mo(g,2p)^{94}Zr	1.79E+06	2.27E-06	Stable
8	^{96}Mo(g,n+p)^{94m}Nb	2.77E+09	3.52E-03	6.26 m
9	^{96}Mo(g,n+p)^{94}Nb	3.80E+08	4.84E-04	2.03E+4 y
10	^{96}Mo(g,2n+p)^{93m}Nb	3.26E+08	4.15E-04	16.12 y
11	^{96}Mo(g,2n+p)^{93}Nb	4.42E+08	5.62E-04	Stable
12	^{96}Mo(g,n+2p)^{93}Zr	1.13E+06	1.43E-06	1.61E+6 y
13	^{96}Mo(g,d)^{94m}Nb	2.05E+08	2.61E-04	6.26 m
14	^{96}Mo(g,d)^{94}Nb	2.54E+07	3.23E-05	2.03E+4 y
15	^{96}Mo(g,t)^{93m}Nb	1.40E+06	1.78E-06	16.12 y
16	^{96}Mo(g,t)^{93}Nb	1.41E+06	1.79E-06	Stable
17	^{96}Mo(g,^{3}He)^{93}Zr	3.05E+04	3.88E-08	1.61E+6 y
18	^{96}Mo(g,a)^{92}Zr	2.06E+09	2.62E-03	Stable

† Normalized reactions rates to ^{100}Mo(g,n)^{99}Mo reaction

Table 12
Calculated reactions rates for ^{95}Mo based on ^{nat}Mo (mAs^{-1} cm^{-3}).

	Reaction	Reaction rate	Normalized reaction rate†	Half-life
1	^{95}Mo(g,n)^{94}Mo	1.48E+12	1.88E+00	Stable
2	^{95}Mo(g,2n)^{93m}Mo	2.26E+08	2.87E-04	6.85 h
3	^{95}Mo(g,2n)^{93}Mo	3.19E+11	4.06E-01	4.0E+3 y
4	^{95}Mo(g,3n)^{92}Mo	1.57E+10	1.99E-02	Stable
5	^{95}Mo(g,p)^{94m}Nb	1.31E+10	1.67E-02	6.26 m
6	^{95}Mo(g,p)^{94}Nb	1.61E+09	2.05E-03	2.03E+4 y
7	^{95}Mo(g,2p)^{93}Zr	4.49E+06	5.71E-06	1.61E+6 y
8	^{95}Mo(g,n+p)^{93m}Nb	2.89E+09	3.67E-03	16.12 y
9	^{95}Mo(g,n+p)^{93}Nb	5.12E+09	6.51E-03	Stable
10	^{95}Mo(g,2n+p)^{92m}Nb	9.39E+08	1.19E-03	10.15 d
11	^{95}Mo(g,2n+p)^{92}Nb	3.45E+08	4.39E-04	3.47E+7 y
12	^{95}Mo(g,n+2p)^{92}Zr	4.64E+06	5.90E-06	Stable
13	^{95}Mo(g,d)^{93m}Nb	9.77E+07	1.24E-04	16.12 y
14	^{95}Mo(g,d)^{93}Nb	1.94E+08	2.46E-04	Stable
15	^{95}Mo(g,t)^{92m}Nb	2.93E+06	3.72E-06	10.15 d
16	^{95}Mo(g.t)^{92}Nb	7.12E+05	9.06E-07	3.47E+7 y
17	^{95}Mo(g,^{3}He)^{92}Zr	7.85E+04	9.99E-08	Stable
18	^{95}Mo(g,a)^{91}Zr	3.96E+09	5.04E-03	Stable

† Normalized reactions rates to ^{100}Mo(g,n)^{99}Mo reaction

Table 13
Calculated reactions rates for ^{94}Mo based on ^{nat}Mo (mAs^{-1} cm^{-3}).

	Reaction	Reaction rate	Normalized reaction rate†	Half-life
1	^{94}Mo(g,n)^{93m}Mo	6.23E+08	7.92E-04	6.85 h
2	^{94}Mo(g,n)^{93}Mo	8.23E+11	1.05E+00	4.0E+3 y
3	^{94}Mo(g,2n)^{92}Mo	1.35E+11	1.72E-01	Stable
4	^{94}Mo(g,3n)^{91m}Mo	3.07E+08	3.91E-04	64.6 s
5	^{94}Mo(g,3n)^{91}Mo	5.97E+08	7.60E-04	15.49 m
6	^{94}Mo(g,p)^{93m}Nb	1.38E+10	1.75E-02	16.12 y
7	^{94}Mo(g,p)^{93}Nb	8.22E+09	1.05E-02	Stable
8	^{94}Mo(g,2p)^{92}Zr	2.89E+07	3.68E-05	Stable
9	^{94}Mo(g,n+p)^{92m}Nb	6.01E+09	7.65E-03	10.15 d
10	^{94}Mo(g,n+p)^{92}Nb	5.26E+08	6.69E-04	3.47E+7 y
11	^{94}Mo(g,2n+p)^{91m}Nb	1.82E+09	2.31E-03	60.86 d
12	^{94}Mo(g,2n+p)^{91}Nb	1.46E+09	1.85E-03	6.8E+2 y
13	^{94}Mo(g,n+2p)^{91}Zr	8.44E+06	1.07E-05	Stable
14	^{94}Mo(g,d)^{92m}Nb	1.42E+08	1.81E-04	10.15 d
15	^{94}Mo(g,d)^{92}Nb	1.28E+07	1.63E-05	3.47E+7 y
16	^{94}Mo(g,t)^{91m}Nb	1.22E+06	1.56E-06	60.86 d
17	^{94}Mo(g,t)^{91}Nb	6.21E+05	7.90E-07	6.8E+2 y
18	^{94}Mo(g,^{3}He)^{91}Zr	3.54E+04	4.50E-08	Stable
19	^{94}Mo(g,a)^{90}Zr	6.53E+09	8.31E-03	Stable

† Normalized reactions rates to ^{100}Mo(g,n)^{99}Mo reaction

Table 14
Calculated reactions rates for ^{92}Mo based on ^{nat}Mo (mAs^{-1} cm^{-3}).

	Reaction	Reaction rate	Normalized reaction rate†	Half-life
1	^{92}Mo(g,n)^{91m}Mo	3.35E+11	4.26E-01	64.6 s
2	^{92}Mo(g,n)^{91}Mo	1.56E+11	1.99E-01	15.49 m
3	^{92}Mo(g,2n)^{90}Mo	1.57E+10	2.00E-02	5.67 h
4	^{92}Mo(g,3n)^{89m}Mo	5.62E+06	7.15E-06	190 ms
5	^{92}Mo(g,3n)^{89}Mo	2.09E+07	2.65E-05	2.11 m
6	^{92}Mo(g,p)^{91m}Nb	4.73E+11	6.02E-01	60.86 d
7	^{92}Mo(g,p)^{91}Nb	6.38E+10	8.11E-02	6.8E+2 y
8	^{92}Mo(g,2p)^{90m}Zr	4.00E+08	5.09E-04	809.2 ms
9	^{92}Mo(g,2p)^{90}Zr	1.47E+10	1.87E-02	Stable
10	^{92}Mo(g,3p)^{89m}Y	3.55E+05	4.51E-07	15.663 s
11	^{92}Mo(g,3p)^{89}Y	5.80E+06	7.38E-06	Stable
12	^{92}Mo(g,n+p)^{90m}Nb	1.16E+10	1.48E-02	18.97 s
13	^{92}Mo(g,n+p)^{90}Nb	6.23E+09	7.92E-03	14.6 h
14	^{92}Mo(g,2n+p)^{89m}Nb	3.24E+08	4.12E-04	66 m
15	^{92}Mo(g,2n+p)^{89}Nb	4.45E+08	5.66E-04	2.03 h
16	^{92}Mo(g,n+2p)^{89m}Zr	2.20E+08	2.80E-04	4.161 h
17	^{92}Mo(g,n+2p)^{89}Zr	2.51E+08	3.20E-04	78.41 h
18	^{92}Mo(g,d)^{90m}Nb	6.20E+07	7.89E-05	18.97 s
19	^{92}Mo(g,d)^{90}Nb	3.23E+07	4.11E-05	14.6 h
20	^{92}Mo(g,t)^{89m}Nb	1.11E+05	1.41E-07	66 m
21	^{92}Mo(g,t)^{89}Nb	1.92E+05	2.44E-07	2.03 h
22	^{92}Mo(g,^{3}He)^{89m}Zr	3.36E+04	4.28E-08	4.161 h
23	^{92}Mo(g,^{3}He)^{89}Zr	1.94E+04	2.47E-08	78.41 h
24	^{92}Mo(g,a)^{88}Zr	4.11E+09	5.23E-03	83.4 d

† Normalized reactions rates to ^{100}Mo(g,n)^{99}Mo reaction

3.4. Final products

The reaction rates and decay equations for each radionuclide produced were used to calculate the atom number and activity concentration at EOB and EOC (2 hours). Appendix B contains a summary of the open channels, reaction products, Q values, reaction threshold energies, decay chains of all radionuclides produced shown in Tables 8 through 14. These calculations were carried out using numerical methods. Table 15 summarizes the atom concentrations, activity concentration, normalized activities at EOB and EOC of all radionuclides produced. A preliminary review of the radioactive products indicates that ^{99}Mo is the primary radionuclide followed by ^{99m}Tc, ^{91m}Nb, ^{90}Nb, ^{96}Nb, ^{91}Mo, and ^{95m}Nb. The specific activity, *SA*, per mA of electron beam current is calculated by dividing the resulting activity with the density of natural molybdenum (10.2 g cm^{-3}). In the present study, the resulting *SA* of ^{99}Mo was 42 GBq g^{-1} mA^{-1} (1.13 Ci g^{-1} mA^{-1}), which is in accordance with previous published results using a 25 MeV LINAC operating at an average current of 0.9 mA (Tur, 2000). Another article indicated a higher *SA* of 10 Ci g^{-1} using a 3-day EOB (Bertsche, 2010). This difference may be due to production methods, LINAC power levels, bremsstrahlung spectrum and target design.

The advantage of using a high-energy electron LINAC is the minimal cooling time required for target processing. By 2 hours, many of the radionuclides decay to insignificant activity levels. However, stable isotopes of molybdenum, niobium, zirconium, and yttrium must to be removed during chemical separation using a

multicolumn selectivity inversion generator (MSIG) followed by further re-concentration of ^{99m}Tc.

Table 15
Calculated activities for radionuclides at end of bombardment (EOB) and end of cooling (EOC) per mA of LINAC electron beam current*.

Decay Product	Atom Concentration at EOB (cm^{-3} mA^{-1})	Activity Concentration at EOB (Bq cm^{-3} mA^{-1})	Normalized Activity	Half life (s)	Normalized Activity at EOC (2 hr)
^{99}Mo	**1.42E+17**	**4.28E+11**	**1.00E+00**	**2.3E+05**	**9.8E-01**
^{93m}Mo	2.81E+13	7.85E+08	1.83E-03	2.5E+04	1.5E-03
^{93}Mo	2.78E+17	1.52E+06	3.55E-06	1.3E+11	3.6E-06
^{91}Mo	4.17E+14	3.09E+11	7.22E-01	9.3E+02	3.4E-03
^{91m}Mo	3.00E+13	3.09E+11	7.22E-01	6.5E+01	2.1E-34
^{89}Mo	3.07E+09	1.69E+07	3.95E-05	1.3E+02	3.0E-22
^{89m}Mo	9.78E+05	3.57E+06	8.34E-06	1.9E-01	0.0E+00
^{99m}Tc	1.05E+16	3.33E+11	7.78E-01	2.2E+04	6.4E-01
^{99}Tc	5.07E+16	5.00E+03	1.17E-08	6.7E+12	1.2E-08
^{97}Zr	3.19E+12	3.57E+07	8.34E-05	6.1E+04	8.0E-05
^{95}Zr	7.62E+10	9.76E+03	2.28E-08	5.4E+06	2.3E-08
^{93}Zr	1.68E+14	3.09E+00	7.22E-12	5.1E+13	7.5E-12
^{90m}Zr	3.86E+08	3.33E+08	7.78E-04	8.1E-01	0.0E+00
^{89m}Zr	5.57E+10	1.55E+08	3.62E-04	2.5E+02	7.7E-13
^{89}Zr	1.64E+14	4.05E+08	9.46E-04	2.8E+05	9.4E-04
^{88}Zr	9.59E+14	9.28E+07	2.17E-04	7.2E+06	2.2E-04
^{99}Nb	1.94E+10	9.04E+08	2.11E-03	1.5E+01	0.0E+00
^{98}Nb	2.10E+09	5.00E+08	1.17E-03	2.9E+00	0.0E+00
^{98m}Nb	7.88E+11	1.79E+08	4.18E-04	3.1E+03	8.3E-05
^{97}Nb	2.32E+13	3.81E+09	8.90E-03	4.3E+03	2.8E-03
^{97m}Nb	1.53E+11	1.81E+09	4.23E-03	5.9E+01	5.1E-40
^{96}Nb	5.83E+14	4.76E+09	1.11E-02	8.4E+04	1.1E-02
^{95}Nb	1.59E+15	3.57E+08	8.34E-04	3.0E+06	8.7E-04
^{95m}Nb	4.93E+14	1.26E+09	2.94E-03	2.7E+05	3.0E-03
^{94}Nb	4.33E+15	4.76E+03	1.11E-08	6.4E+11	1.1E-08
^{94m}Nb	8.12E+12	1.50E+10	3.50E-02	3.8E+02	6.0E-08
^{93m}Nb	3.97E+15	5.47E+06	1.28E-05	5.1E+08	1.3E-05
^{92}Nb	1.70E+14	1.07E-01	2.50E-13	1.1E+15	2.6E-13
^{92m}Nb	1.33E+15	1.05E+09	2.45E-03	8.8E+05	2.5E-03
^{91}Nb	1.03E+17	3.33E+06	7.78E-06	2.1E+10	7.9E-06
^{91m}Nb	1.49E+17	1.98E+10	4.63E-02	5.3E+06	4.7E-02
^{90}Nb	1.32E+15	1.74E+10	4.07E-02	5.3E+04	3.8E-02
^{90m}Nb	6.97E+14	2.62E+13	6.12E+01	1.9E+01	0.0E+00
^{89}Nb	3.36E+12	3.09E+08	7.22E-04	7.3E+03	3.8E-04
^{89m}Nb	1.30E+12	2.28E+08	5.33E-04	4.0E+03	1.5E-04
^{89m}Y	5.38E+06	2.38E+05	5.56E-07	1.6E+01	0.0E+00
^{88}Y	1.10E+13	8.33E+05	1.95E-06	9.2E+06	2.0E-06

* Stable isotopes have been omitted. These are ^{98}Mo, ^{97}Mo, ^{96}Mo, ^{95}Mo, ^{94}Mo, ^{92}Mo, ^{99}Ru, ^{89}Y, ^{93}Nb, ^{92}Zr, ^{91}Zr, ^{90}Zr, ^{89}Y, and ^{88}Sr.

3.5. Radiological safety

Production of high-energy photons and neutrons is of significant concern in radiological safety. The design of a facility requires adequate shielding for workers and members of the public. The structural shielding design was based on recommendations as described in NCRP Report 151 "Structural Shielding Design And Evaluation For Megavoltage X- And Gamma-Ray Radiotherapy Facilities," (NCRP, 1964, 2005). Based on 10 CFR 20.1301, the total effective dose equivalent to individual members of the public shall not exceed 0.1 rem (1 mSv) per year. Moreover, the dose in any unrestricted area from external sources shall not exceed 0.002 rem (0.02 mSv) in any one hour. Based on these dose limits it is necessary to assess the shielding requirements for a high-energy electron LINAC facility.

3.5.1. Neutron shielding

The cross sections for photo-neutron production for natural molybdenum and tungsten were calculated using the TALYS computer code (Koning and Rochman, 2012). Fig. 13 shows the cross sections and neutron yields as a function of photon energy for molybdenum and tungsten. Based on the bremsstrahlung spectrum generated by the LINAC, the calculated total neutron yield was 1.86×10^{13} s^{-1} mA^{-1} and 5.75×10^{13} s^{-1} mA^{-1} for natural molybdenum and tungsten, respectively. The selected shielding material for photons and neutrons is borated-lead polyethylene or zirconium borohydride, $Zr(BH_4)_4$

concrete with a density of 3.8 g cm^{-3} and 1.18 g cm^{-3} respectively (Hayashi et al., 2009). However, polyethylene is considered a fire hazard around high-powered LINACS and consideration of polyethylene was discarded.

Neutrons are generated forward peaked, therefore shielding calculations should be based on the same photon angular distribution using Eq. (2.5). The dose equivalent per unit fluence, P_H, conversion factors were obtained from NCRP Report 38 (NCRP, 1971*)*, and applied as described by Cossairt and Vaziri (Cossairt and Vaziri, 2009). Thus, based on the neutron attenuation properties of $Zr(BH_4)_4$, and a total neutron fluence rate at 1 meter of 7.61 $\times 10^9$ cm^{-2} s^{-1} mA^{-1}, the required thickness to attenuate neutrons to a satisfactory dose limit of 0.02 mSv per hour was 89 cm.

3.5.2. Bremsstrahlung shielding

Photon attenuation calculations were carried out using the high-energy bremsstrahlung spectrum obtained using the Monte Carlo transport code MCNP. The linear attenuation coefficients for $Zr(BH_4)_4$ as a function of energy were obtained from the online database XCOM: Photon Cross Sections Database (NIST, 2017). The absorbed dose was calculated and the wall thickness was estimated based on the corresponding dose limit of 0.02 mSv per hour. The resulting thickness estimate was found to be 200 cm. Consequently, bremsstrahlung was found to be the primary concern in shielding design for the high-energy LINAC. The total shielding using $Zr(BH_4)_4$ with a thickness of 200 cm will suffice to comply with the dose limits.

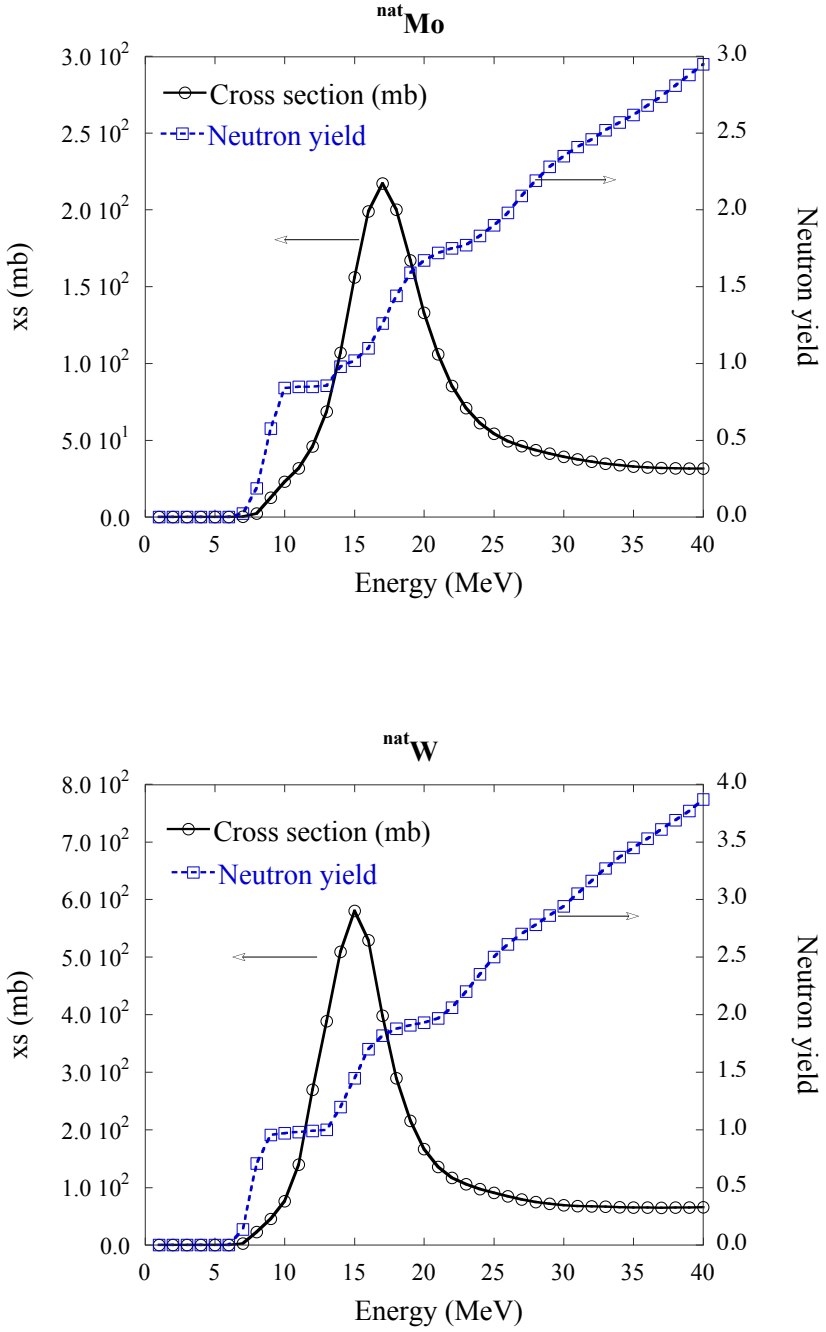

Fig. 13. Cross sections and neutron yields as a function of photon energy for the ^{nat}Mo(γ,x)n and ^{nat}W(γ,x)n.

4. DISCUSSION

4.1. Comparison between proposed and current production methods

The use of a high-energy LINAC for the production of ^{99}Mo via ^{100}Mo(γ,n)^{99}Mo is an appealing strategy as an alternative method when compared to those methods requiring the use of HEU and LEU (Fig. 2). In the present study the final calculated specific activity of ^{99}Mo was 42 GBq g^{-1} mA^{-1} (1.13 Ci g^{-1} mA^{-1}), which is four orders of magnitude lower than that obtained using HEU in nuclear reactors (Lewis, 1971). However, taking into account the cost of a nuclear reactor, radioactive waste handling and disposal, operational costs and maintenance, and decommissioning of nuclear facilities, makes nuclear reactor production methods unappealing. The current capital cost for dedicated medical radionuclide production facility using HEU or LEU is estimated to be $500 million (World Nuclear News, 2015). The National Nuclear Security Administration (NNSA) has awarded more than $25 million to support projects focusing on domestic development of ^{99}Mo production without the use of HEU or LEU.

When compared with the production method based on neutron capture via ^{98}Mo(n, γ)^{99}Mo, the neutron fluence rate required to achieve the same reaction rate obtained using ^{100}Mo(γ,n)^{99}Mo will be 4x10^{14} cm^{-2} s^{-1}, which can be attained in nuclear reactors with an operating power higher than 20 MW. Therefore, this will require a significant financial investment.

Accelerator induced fission via $^{235}U(n,f)$ using thermalized neutrons produced by an accelerator is quite inefficient as these accelerators produce high-energy neutrons with a fluence rate in the order of 10^{12} s^{-1} using D-D or D-T reactions. The thermalization of neutrons requires a moderator, thus reducing the fluence rate as distance is increased from the target by 4 orders of magnitude. Current commercial neutron generator can produce a fluence rate of 10^{14} n s^{-1} and require the use of polyethylene blankets to thermalize neutrons. This approach however, has not been explored to a great extent.

The direct production of ^{99m}Tc has also been considered for those hospitals that have a high-energy cyclotron using the $^{100}Mo(p,2n)^{99m}Tc$. This approach is very appealing for internal production and use of ^{99m}Tc. However, for commercialization, this approach is financially unfeasible unless production of other radionuclides is considered. An advantage of the present strategy is the minimal mass required of highly enriched ^{100}Mo to be deposited in a target disk where the proton incident entry and exit energy is 24 MeV and 10 MeV, respectively. The result is an effective target thickness of 0.085 cm. This target thickness will result in a high specific activity that minimizes the use and cost of ^{100}Mo, which needs to be recycled after every chemical separation. As with the present production method, heat dissipation in the target disk becomes a significant issue. The heat generated per mA of current over a 1-cm^2 disk with thickness of 0.085 cm will result in 14 kW-mA^{-1}. Therefore, cooling the back of the target becomes a significant challenge in order to maintain target integrity. Both the present strategy using $^{nat}Mo(\gamma,n)^{99}Mo$ and the direct approach of producing ^{99m}Tc create impurities of Nb, Zr,

and Y, which must be removed using a multicolumn selectivity inversion generator (MSIG) to comply with USP <797>.

Overall, all present strategies using accelerators or cyclotrons have their benefits and limitations. Minimizing the cost of production, chemical separation and establishing a FDA Drug Master File (DMF) for commercialization are significant challenges (FDA, 1989).

4.2. Chemical separation of impurities

The separation of chemical impurities (radioactive and non-radioactive) is essential to maintain quality control, radionuclidic purity and specific activity. The development of generators for use with low specific activity of ^{99}Mo is a challenge. The IAEA has established a coordinated research study (CRS) for the development of novel gel generators for low ^{99}Mo specific activity using low enriched uranium (LEU) or neutron activation (IAEA, 2015). Gel generators can be applied in the present strategy in place of high-capacity adsorbents used in multicolumn selectivity inversion generator (MSIG). In 2016, the IAEA established a CRP group dedicated to investigating new strategies for chemical separation and production of new generators using the present strategy with low ^{99}Mo specific activity. The CRP title is "New Ways of Producing Technetium-99m (Tc-99m) and Tc-99m Generators." The objective of the CRP study was to evaluate new ways of producing ^{99m}Tc, such as the present strategy via the

$^{100}Mo(\gamma,n)^{99}Mo$ reaction, and establish new $^{99}Mo/^{99m}Tc$ generators using low specific activity ^{99}Mo.

Thus, the choice for chemical separation and generation production will be based on gel separation and high-capacity adsorbents. Therefore, this new designs will bring a paradigm shift in the way $^{99}Mo/^{99m}Tc$ is being distributed as they will be more complex requiring further quality control at the clinical site.

5. CONCLUSIONS

The present study carried out an analysis for the production of ^{99}Mo via photonuclear reactions with natural molybdenum using the NIRTA tragetry system. The optimal energy of the electron LINAC was found to be 40 MeV. All potential open channels were analyzed and corresponding reaction rates and decay schemes were calculated to assess final activities at EOB and EOC. The estimated specific activity for a nominal 3-day irradiation was 42 GBq g^{-1} mA^{-1} (1.13 Ci g^{-1} mA^{-1}) at EOB. The resulting stable impurities, excluding stable Mo isotopes, were ^{99}Ru, ^{89}Y, ^{93}Nb, ^{92}Zr, ^{91}Zr, ^{90}Zr, ^{89}Y, and ^{88}Sr. The primary radioactive impurities were ^{91m}Nb, ^{90}Nb, ^{96}Nb, ^{91}Mo, and ^{95m}Nb. The present study confirms the feasibility of using a high-energy LINAC for the production of ^{99}Mo via ^{100}Mo(γ,n)^{99}Mo with minimal and manageable impurities, that could be removed using a gel separation method and multicolumn selectivity inversion generator (MSIG).

REFERENCES

Atcher, R.W., Berridge, M.S., Boros, E., Brown, R.W., Cutler, C.S., SNMMI, 2016. USP Public Standards for Compounded Sterile Radiopharmaceuticals Recommendations from SNMMI, in: SNMMI (Ed.). SNMMI.

Bakel, A.J., Aase, S.B., Quigley, K.J., Vandegrift, G.F., 2004. Thermoxid sorbents for the separation and purification of Mo-99, 26th International Meeting on Reduced Enrichment for Research and Test Reactors, Vienna, Austria.

Ballinger, J.R., 2010. Mo-99 shortage in nuclear medicine: crisis or challenge? *Journal of Labelled Compounds and Radiopharmaceuticals* 53, 167-168.

Beaver, J.E., Hupf, H.B., 1971. Production of Tc-99m on a medical cyclotron: a feasibility study. *J Nucl Med* 12, 739-741.

Bertsche, K., 2010. Accelerator Production Options for Mo-99. SLAC National Accelerator Laboratory (SLAC).

ChinaTungsten, 2017. High Density Molybdenum Target Production Processes, http://www.molybdenum.com.cn/high-density-molybdenum-target-production-processes.html.

Cossairt, J.D., Vaziri, K., 2009. Neutron Dose Per Fluence and Weighting Factors for Use at High Energy Accelerators. *Health Phys* 96, 617-628.

Cuttler, J.M., 2010. Producing Mo-99 in CANDU Reactors, Canadian Nuclear Society, Montreal, Quebec.

Danon, Y., Block, R., Harvey, J., 2010. Production of Mo-99 using 30-MeV electrons and a Mo-100 target. Transactions of the American Nuclear Society 103, 1081-1082.

Dash, A., Chakravarty, R., 2014. Pivotal role of separation chemistry in the development of radionuclide generators to meet clinical demands. RSC Advances 4, 42779-42803.

Dash, A., Chakravarty, R., Ram, R., Pillai, K.T., Yadav, Y.Y., Wagh, D.N., Verma, R., Biswas, S., Venkatesh, M., 2012. Development of a 99Mo/99mTc generator using alumina microspheres for industrial radiotracer applications. *Appl Radiat Isot* 70, 51-58.

Dash, A., Knapp, F.F., Jr., Pillai, M.R., 2013. Mo-99/Tc-99m separation: an assessment of technology options. *Nucl Med Biol* 40, 167-176.

Dutch, D.N., 2014. "Safety procedures ignored" at Petten nuclear reactor: investigation, Dutch News. Dutch News, Netherlands.

Eckelman, W., Richards, P., 1970. Instant Tc-99m DTPA. *J Nucl Med* 11, 761.

FDA, 1989. Drug Master Files: Guidelines. Center for Drug Evaluation and Research. Food and Drug Administration, Rockville, MD.

Goorley, T., 2012. Initial MCNP6 Release Overview. *Nuclear technology* 180, 298-315.

Hayashi, T., Tobita, K., Nakamori, Y., Orimo, S., 2009. Advanced neutron shielding material using zirconium borohydride and zirconium hydride. *J Nucl Mater* 386-88, 119-121.

IAEA, 1987. Fission Molybdenum for Medical Use, Technical Committee Meeting IAEA. IAEA, Karlsruhe.

IAEA, 2006. Cumulative Fission Yields, in: Koning, A., Forrest, R., Kellet, M., Mills, R., Henriksson, H., Rugama, Y. (Eds.), Joint Evaluated Fission and Fusion File, Incident-neutron data. https://www-nds.iaea.org/sgnucdat/c3.htm, Paris, France.

IAEA, 2008. Homogeneous aqueous solution nuclear reactors for the production of Mo-99 and other short lived radioisotopes.

IAEA, 2013. Non-HEU Production Technologies For Molybdenum-99 And Technetium-99m, IAEA Nuclear Energy Series. International Atomic Energy Agency, Vienna, Austria.

IAEA, 2015. Feasibility of Producing Molybdenum-99 on a Small Scale Using Fission of Low Enriched Uranium or Neutron Activation of Natural Molybdenum. International Atomic Energy Agency, Vienna, Austria.

Kastango, E.S., Weatherman, K.D., 2010. Addressing <797> Requirements for Radiopharmaceuticals, Pharmacy Purchasing and Products. pppmag.com, WEB, p. 3.

Koning, A.J., Rochman, D., 2012. Modern Nuclear Data Evaluation with the TALYS Code System. Nuclear Data Sheets 113, 2841-2934.

Koning, A.J., Rochman, D., Kopecky, J., Sublet, J.C., Bauge, E., Hilaire, S., Romain, P., Morillon, B., Duarte, H., van der Marck, S., Pomp, S., Sjostrand, H., Forrest, R., Henriksson, H., Cabellos, O., Goriely, S., Leppanen, J., Leeb, H., Plompen and R. Mills, A., 2015. TENDL-2015: TALYS-based evaluated nuclear data library.

Kosako, K., Oishi, K., Nakamura, T., Takada, M., Sato, K., Kamiyama, T., Kiyanagi, Y., 2010. Angular Distribution of Bremsstrahlung from Copper and Tungsten Targets Bombarded by 18, 28, and 38 MeV Electrons. *Journal of Nuclear Science and Technology* 47, 286-294.

Koster, U., 2013. Present day production of Mo-99 and alternatives, Nuclear Instruments and Methods Research, Institut Laue Langevin, Grenoble France.

Lepora, N., 2006. *Molybdenum*. Cavendish Square Publishing, New York, NY, United States.

Lewis, R.E., 1971. Production of High Specific Activity Molybdenum-99 for Preparation of Technetium-99m Generators. *Int J Appl Radiat* Is 22, 603-609.

May, I., Rios, D., Anderson, A.S., Bitteker, L.J.J., Copping, R., Dale, G.E., Dalmas, D.A., Gallegos, M.J., Garcia, E., Kelsey, C.T.I., Mocko, M., Reilly, S.D., Stephens, F.H., Taw, F.L., Woloshun, K.A., 2013. A Technical Demonstration of the Initial Stage of Mo-99 Recovery from a Low Enriched Uranium Sulfate Solution. Los Alamos National Laboratory, Los Alamos, NM.

Messick, C., Galan, J., 2013. Global Threat Reduction Initiative. U.S. DOE, 11.

Nagai, Y., Hatsukawa, Y., 2009. Production of Mo-99 for Nuclear Medicine by Mo-100(n,2n)Mo-99. *Journal of the Physical Society of Japan* 78, 033201.

NAS, 2016. Molybdenum-99 for Medical Imaging. National Academy of Sciences, Washington, D.C.

NCRP, 1964. Shielding for high-energy electron accelerator installations; recommendations of the National Council on Radiation Protection and Measurements, NCRP Report No. 97. National Bureau of Standards, Washington, DC.

NCRP, 1971. Protection against neutron radiation: recommendations of the National Council on Radiation Protection and Measurements, NCRP Report No. 38. National Council on Radiation Protection and Measurements, Washington, DC.

NCRP, 2005. Structural shielding design and evaluation for megavoltage x- and gamma-ray radiotherapy facilities: recommendations of the National Council on Radiation Protection and Measurements, NCRP Report No. 151, Washington, DC.

NIST, 2017. XCOM: Photon Cross Sections Database. National Institute of Standards and Technology.

NNDC, 2017. Q-value Calculator. http://www.nndc.bnl.gov/qcalc/.

Nordell, B., Brahme, A., 1984. Angular distribution and yield from bremsstrahlung targets (for radiation therapy). *Physics in medicine and biology* 29, 797-810.

NRC, 2009. Medical isotope production without highly enriched uranium. National Academies Press, Washington, D.C.

OECD, N.E.A., 2010. Review of Potential Molybdenum-99/Technetium-99m Production Technologies, The Supply of Medical Radioisotopes. Organization for Economic Co-operation and Development.

Pramudita, A., 2011. Linacs for Medical Isotope Production. *Atom Indonesia* 37, 1-4.

Raj Prakash, H.G., Sanjeev, G., Vijay Kumar, K.B., Harish Kumar, H.G., Siddappa, K., Nayak, B.K., Saxena, A., 2011. Measurement of Photofission Cross-Section of U-238 Using Microtron Facility. *International Journal of Modern Physics* Volume 20, 2361-2375.

Sarkar, S.K., Kothalkar, C., Naskar, P., Joshi, S., Saraswathy, P., Dey, A.C., Vispute, G.L., Murhekar, V.V., Pilkhwal, N., 2013. Indigenous technology development and standardization of the process for obtaining ready to use sterile sodium pertechnetate-Tc-99m solution from Geltech generator. *Indian J Nucl* Med 28, 70-74.

Seaborg, G.T., Segre, E., 1939. Nuclear isomerism in element 43. *Phys* Rev 55, 0808-0814.

Segre, E., Seaborg, G.T., 1938. Nuclear isomerism in element 43. *Phys* Rev 54, 772-772.

Segre, E., Wu, C.S., 1940. Some fission products of uranium. *Phys* Rev 57, 552-552.

Selek, S., Coban, A., Boztosun, I., Dapo, H., Karakoc, M., 2015. Photofission of U-238 Nuclei. *Journal of Physics* 590.

Sigma-Aldrich, 2017. Molybdenum Powder, in: http://www.sigmaaldrich.com/catalog/product/aldrich/266892?lang=en&region=US (Ed.).

Soppera, N., Bossant, M., Dupont, E., 2014. JANIS 4: An Improved Version of the NEA Java-based Nuclear Data Information System. *Nuclear Data Sheets* 120, 294-296.

Starovoitova, V.N., Tchelidze, L., Wells, D.P., 2014. Production of medical radioisotopes with linear accelerators. *Appl Radiat Isot* 85, 39-44.

Takada, M., Kosako, K., Oishi, K., Nakamura, T., Sato, K., Kamiyama, T., Kiyanagi, Y., 2013. Angular distributions of absorbed dose of Bremsstrahlung and secondary electrons induced by 18-, 28- and 38-MeV electron beams in thick targets. *Radiat Prot Dosimetry* 153, 369-383.

Tollesfon, J., 2016. Reactor Shutdown Threatens World's Medical Isotope Supply. *International Weekly Journal of Science* web.

Tur, Y.D., 2000. Linear Electron Accelerator for the Medical Isotopes Production, 7th European Particle Accelerator Conference. EPAC, Vienna, Austria, pp. 2560-2562.

Wilk, A., 2016. Sodium Pretechnetate Tc-99m Injection, USP Monographs. USP 29, United States Pharmacopeia.

World Nuclear News, 2015. US firms target revival in domestic Mo-99 production. World Nuclear Association, London.

Yilmaz, E., Baltas, H., Kiris, E., Ustabas, I., Cevik, U., El-Khayatt, A.M., 2011. Gamma ray and neutron shielding properties of some concrete materials. Ann Nucl Energy 38, 2204-2212.

APPENDIX A

The bremsstrahlung spectrum generated by the high-energy electron linear accelerator was calculated using the Monte Carlo transport code MCNP6. The geometry used in the simulation was based on the NIRTA targetry system for a single molybdenum target disk. The tungsten target disk had a diameter of 12.6 mm and a height of 2.5 mm. The molybdenum disk had a diameter of 12.6 mm and a height of 2.0 mm. The separation between the tungsten and molybdenum disks was 0.87 cm. Figures A1 through A5 show different sections and cross sectional views of the NIRTA targetry system.

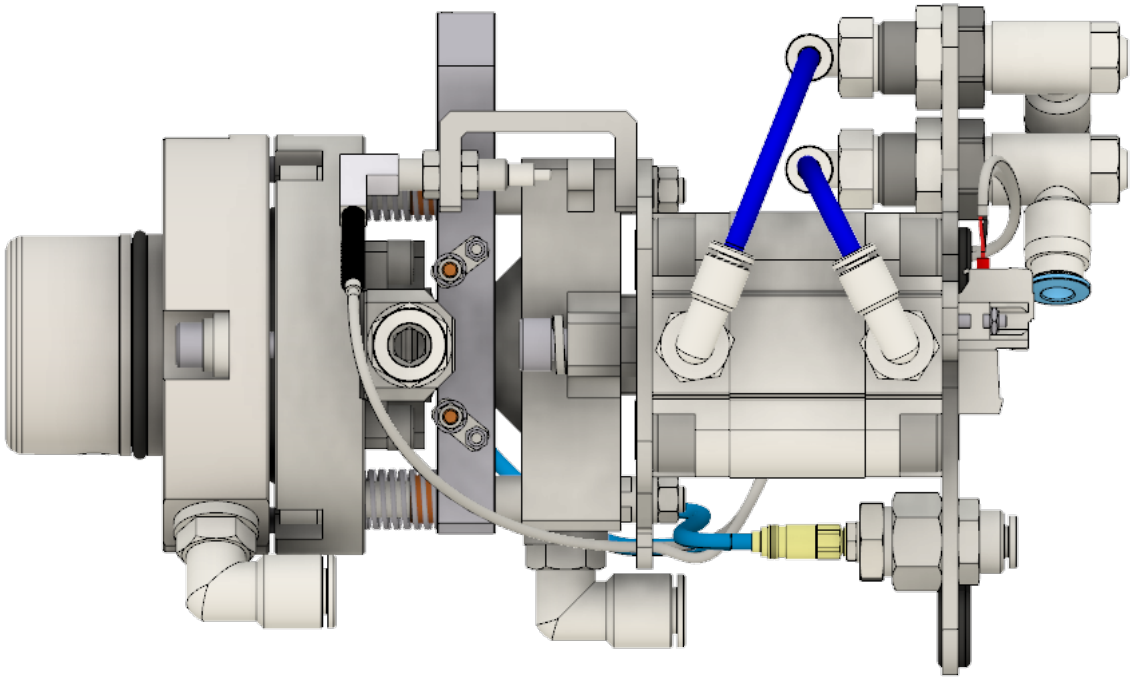

Fig. A1. General overview NIRTA targetry system used for the irradiation of molybdenum targets.

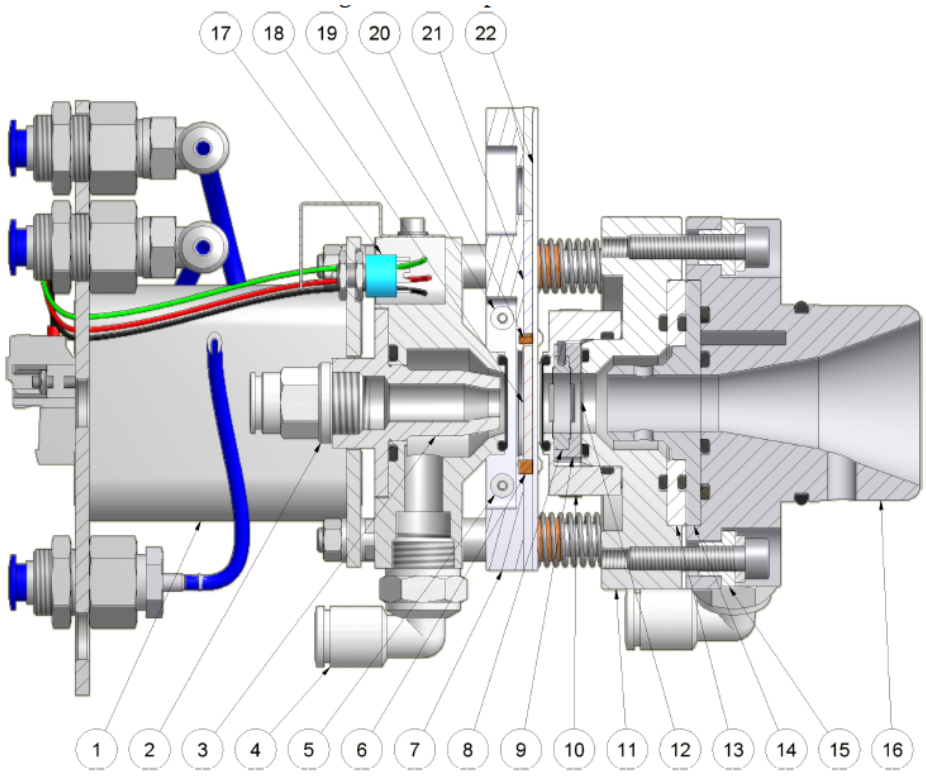

Fig. A2. Cross sectional view of NIRTA targetry system showing its different components:

1 – pneumatic cylinder driving the water cooling jet assembly;

2 – inlet fitting for the cooling water jet;

3 – nozzle for creating the water jet for cooling the back of the target disk;

4 – outlet fitting for the cooling water;

5 – miniature cylinder for driving the locking tongue;

6 – target locking tongue;

7 – target guiding plate;

8 – cooling cavity's inner insert;

9 – cooling cavity's outer insert;

10 – cooling cavity;

11 – connection body;

12 – window foil for tungsten target;

13 – PEEK insulator ring;

14 – aluminum extension of the collimator;

15 – PEEK insulator insert;

16 – quick connection flange for mounting to high energy electron accelerator extended target ports, with integrated ⍰12 mm beam collimator made of aluminum;

17 – microswitch;

18 – target disk in irradiation position;

19 – miniature cylinder for driving the intercepting tongue;

20 – intercepting tongue;

21 – second target disk in queue;

22 – third target disk in queue.

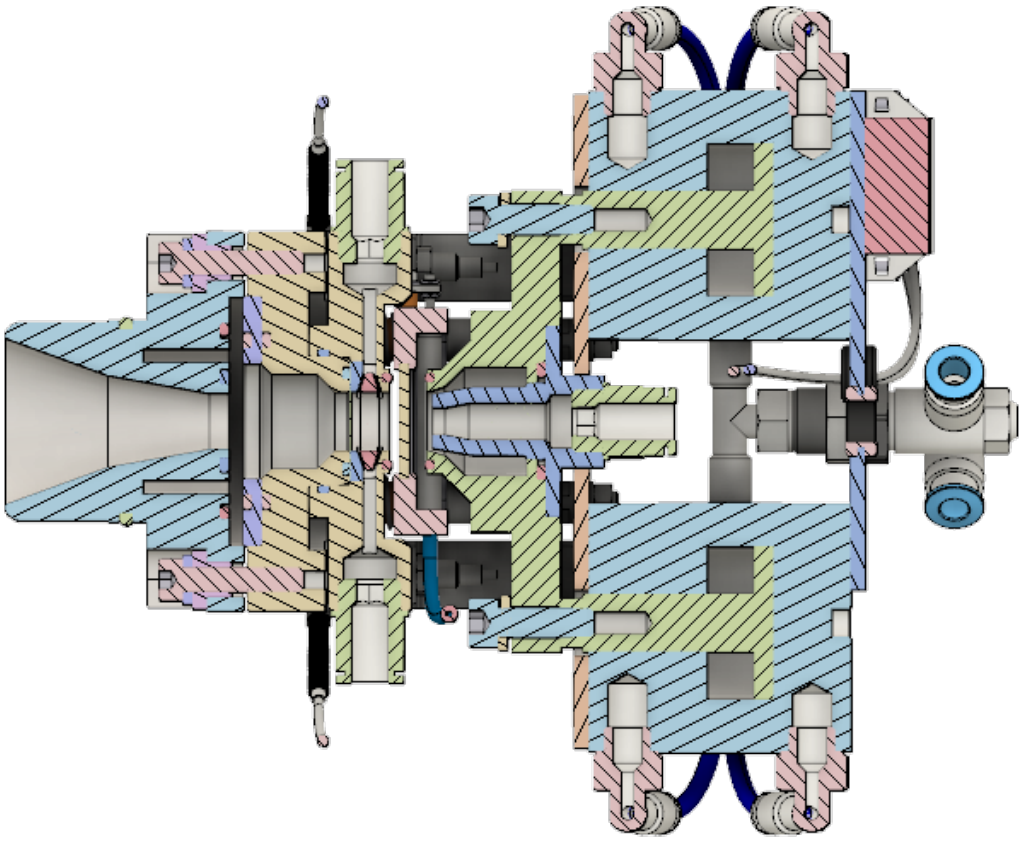

Fig. A3. Cross sectional view of NIRTA targetry system showing the different sections of the back disk water jet cooling, front

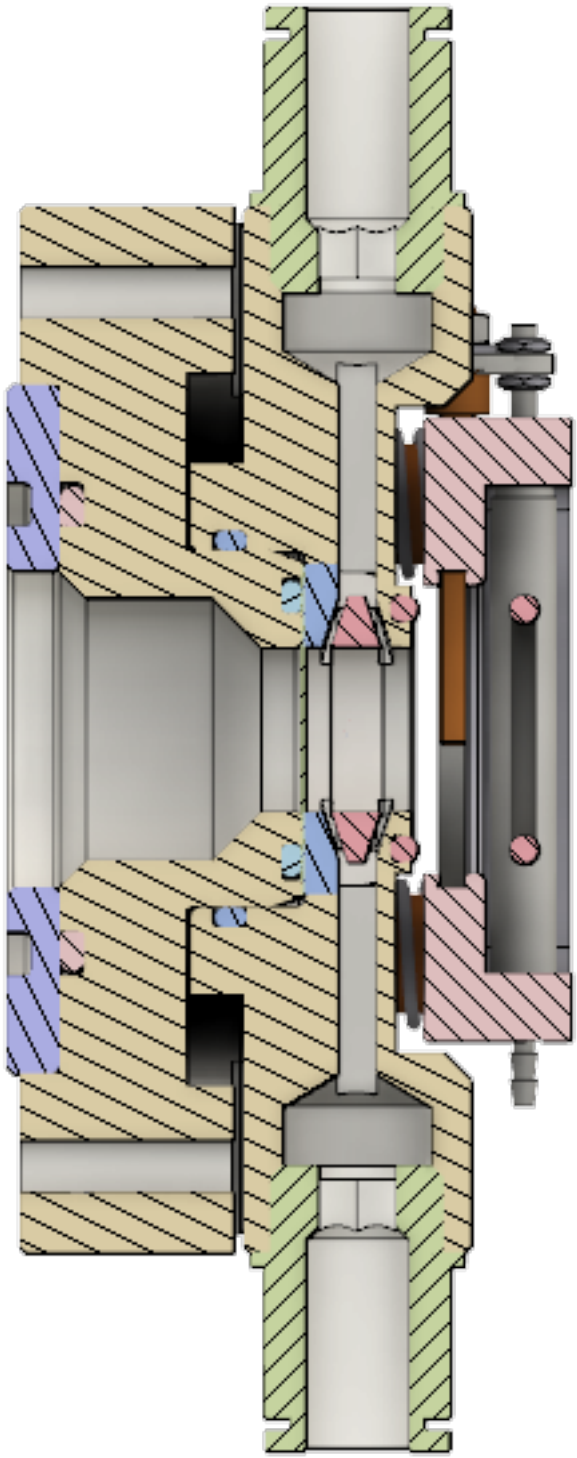

Fig. A4. Cross sectional view of tungsten and molybdenum targets with the cooling lines for heat dissipation.

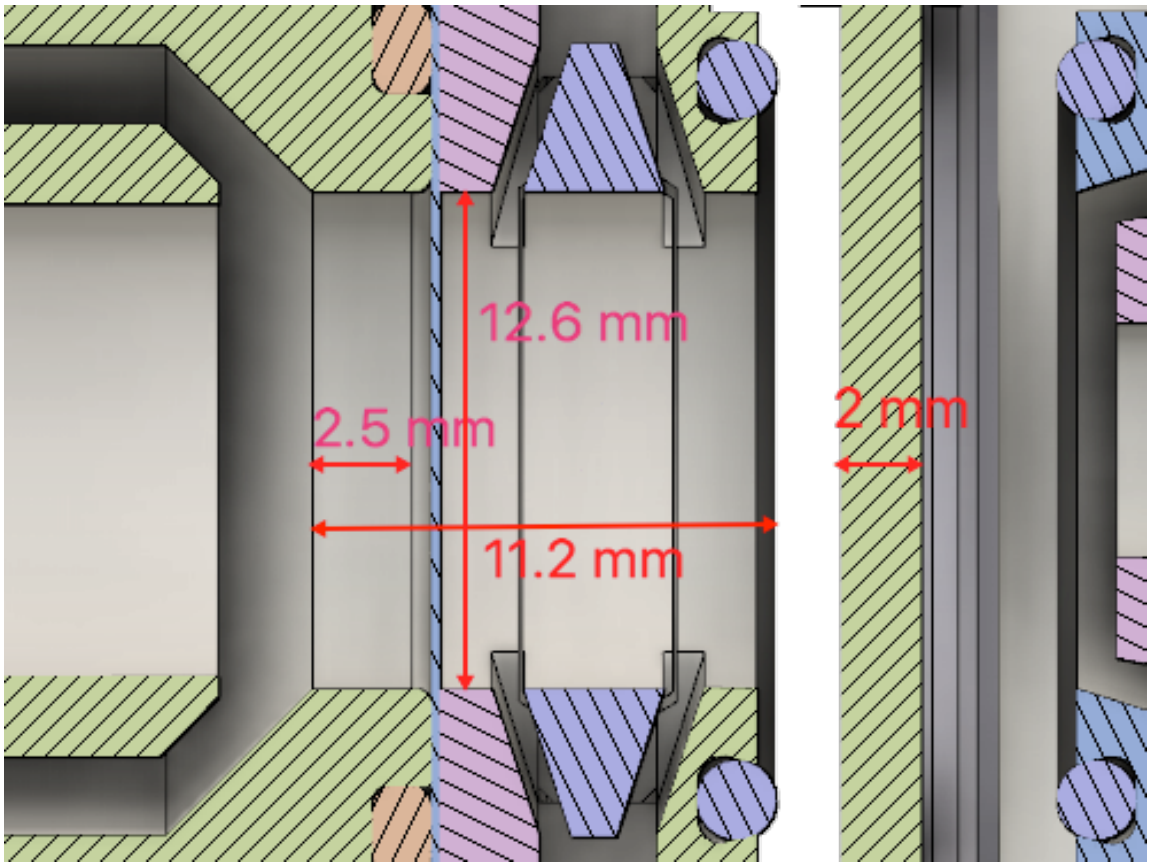

Fig. A5. Close cross sectional view and dimensions of tungsten and molybdenum targets with the cooling lines for heat dissipation.

The MCNP code used to calculate the bremsstrahlung spectrum from high-energy electrons is given below. This code was used to calculate the spectrum produced by 30, 35, 40, and 45 MeV electrons. The geometry used in the code was that given in Fig. A5.

Monte Carlo transport code (MCNP6(used to calculate the bremsstrahlung spectrum generated by the high-energy electron linear accelerator.

```
Bremsstrahlung production 40 MeV electrons
C ------------------------------------------------------------------------------
C Cells
C ------------------------------------------------------------------------------
1000  20 -19.3       -11 12 -13                      imp:e=1 imp:p=1       $ disk of
tungsten
1100  30 -10.22      -11 14 -15                      imp:e=1 imp:p=1       $ disk of
molybdenum
1200  10 -0.00000001 -10 16 -17 #1000 #1100         imp:e=1 imp:p=1       $ inner region
of the target
9999   0                 10:-16:17                  imp:e=0 imp:p=0       $ cylinder

C ------------------------------------------------------------------------------
C Surfaces
C ------------------------------------------------------------------------------
10   CZ 10.0    $ Cylinder of radius of 10.0 cm Domain
11   CZ 0.5              $ Cylinder of radius of 0.5 cm
12   PZ 0.0     $ Z-plane representing the bottom of the tungsten target
13   PZ 0.25    $ Z-plane representing the top of the tungsten target
14   PZ 1.12     $ Z-plane representing the bottom of the molybdenum target
15   PZ 1.32     $ Z-plane representing the top of the molybdenum target
16   PZ -5.0    $ Z-plane representing the bottom of the domain cyclinder
17   PZ 5.0     $ Z-plane representing the top of the domain cyclinder

C ------------------------------------------------------------------------------
C Data
C ------------------------------------------------------------------------------
MODE P E
SDEF POS=0 0 0 AXS=0 0 1 RAD=d1 PAR=3 ERG=40 VEC=0 0 1 DIR=1
SI1 0 0.5                                          $ radial sampling range: 0 to Rmax = 0.5
cm
SP1 -21 1                                          $ radial sampling weighting: r^1 for disk
c ---------------------------------------------------------
c WATER for electron and photon transport (by mass fraction)
c ---------------------------------------------------------
M10  1000 2                                        $ elemental H and atomic abundance
         8000 1                                    $ elemental O and atomic abundance
C Tungsten
```

```
M20      74000 1
C Molybdenum
M30  42000 1
F4:P 1100
E4 1 2 3 4 5 6 7 8 9 10 11 12 13 14 15 16 17 18 19 20 21 22 23 24
     25 26 27 28 29 30 31 32 33 34 35 36 37 38 39 40 41 42 43 44 45 $ energy bin
boundaries
NPS  1E5
```

APPENDIX B

The production of different radionuclides produced during the irradiation of natural molybdenum are governed by the corresponding reaction rate for each open channel, the abundance of each molybdenum isotope, which are proportional to the photon fluence rate and cross sections for each open channel. For a given open channel, the microscopic reaction rate, *rr*, is calculated as

$$rr = \int s(E)\sigma(E)dE\,, \tag{B1}$$

where $s(E)$ is the photon fluence rate expressed in units of cm^{-2} mAs^{-1}, and $\sigma(E)$ is expressed in cm^2 per atom. The photon fluence rate was calculated using the MCNP Monte Carlo code based on the geometry of the NIRTA targetry system. The macroscopic reaction rate, *RR*, is given as the product of the microscopic reaction rate, *rr*, and the atom density for a given isotope (and corresponding natural abundance), and is given as

$$RR = N_T \cdot rr\,, \tag{B1}$$

where

$$N_i = \frac{N_A \cdot \rho}{M} f_i\,, \tag{B2}$$

and N_A is Avogadro's number, ρ is the density (g cm^{-3}), *M* is the molecular weight (g mol^{-1}), and f_i is the natural abundance of the isotope.

The macroscopic reaction rate is used in the decay equations for every potential radionuclide produced during bombardment. The decay equations were utilized to

determine the stable and radioactive daughters produced during activation of natural molybdenum. The decay equations are needed for assessing the ultimate activity levels for each potential radionuclide and for establishing the procedures for chemical separation.

The reaction rate in conjunction with decay constants for the respective radionuclides were used to calculate the final activity for each potentially produced radionuclide at the end of bombardment and after cooling period to allow for the decay of short lived radionuclides.

$$\begin{aligned}
\frac{dN_1}{dt} &= RR - \lambda_1 N_1 \\
\frac{dN_2}{dt} &= \lambda_1 N_1 - \lambda_2 N_2 \\
\frac{dN_3}{dt} &= \lambda_2 N_2 - \lambda_3 N_3 \quad , \\
&\vdots \\
\frac{dN_i}{dt} &= \lambda_{i-1} N_{i-1} - \lambda_i N_i
\end{aligned} \tag{B3}$$

where N_i is the number of atoms per unit volume of target for the parent and subsequent daughter radionuclides and λ_i is the corresponding physical decay constant (i = 1, 2, 3).

The reactions presented below represent the open channels with threshold energies below 40 MeV and normalized reaction rates below 1×10^{-8}. The Q values and threshold energies, E_{th} (keV) were obtained from the National Nuclear Data Center (NNDC, https://www.nndc.bnl.gov/qcalc/index.jsp). Potential open channels with threshold energies above 40 MeV were not considered in the present analysis.

^{100}Mo Reactions

Production of ^{99}Mo via photo-neutron reaction with ^{100}Mo

$$^{100}Mo(\gamma,n)^{99}Mo$$

Q-value (keV): -8291.83 Threshold (keV): 8292.19

$$^{99}Mo \xrightarrow[65.976\ h]{\beta} \begin{cases} \xrightarrow{12.2\%} {}^{99}Tc \xrightarrow[2.1E+5\ y]{\beta} {}^{99}Ru \\ \xrightarrow{87.8\%} {}^{99m}Tc \xrightarrow[6.02\ h]{\beta} {}^{99}Tc \xrightarrow[2.1E+5\ y]{\beta} {}^{99}Ru \end{cases}$$

Ruthenium-99 is stable

Production of ^{98}Mo via gamma-2-neutron reaction with ^{100}Mo

$$^{100}Mo(\gamma,2n)^{98}Mo$$

Q-value (keV): -14217.27 Threshold (keV): 14218.35

Molybdenum-98 is stable

Production of ^{97}Mo via gamma-3-neutron reaction with ^{100}Mo

$$^{100}Mo(\gamma,3n)^{97}Mo$$

Q-value (keV): -22859.87 Threshold (keV): 22862.68

Molybdenum-97 is stable

Production of ^{99}Nb via gamma-proton reaction with ^{100}Mo

$$^{100}Mo(\gamma,p)^{99}Nb$$

Q-value (keV): -11146.7 Threshold (keV): 11147.3

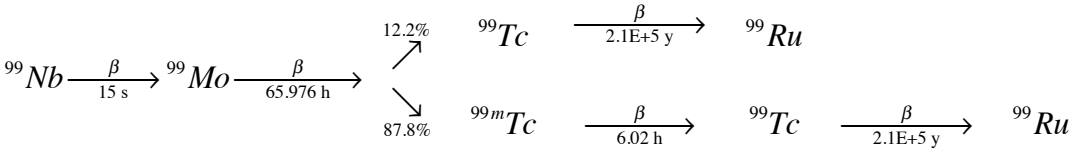

Ruthenium-99 daughter is stable

Production of ^{89}Zr via gamma, 2-proton reaction with ^{100}Mo

$$^{100}Mo(\gamma,2p)^{89}Zr$$

Q-value (keV): -19474.91 Threshold (keV): 19476.95

$$^{89}Zr \xrightarrow[78.41h]{\beta+} {}^{89}Y$$

Yttrium-89 daughter is stable

Production of ^{97}Y via gamma, 3-proton reaction with ^{100}Mo

$$^{100}Mo(\gamma,3p)^{97}Y$$

Q-value (keV): -31929.2 Threshold (keV): 31934.68

$$^{97}Y \xrightarrow[3.75\,s]{\beta-} {}^{97}Zr \xrightarrow[16.75\,h]{\beta-} {}^{97}Nb \xrightarrow[72.1\,\mathrm{min}]{\beta-} {}^{97}Mo$$

Molybdenum-97 daughter is stable

Production of ^{98m}Nb via gamma, neutron+proton reaction with ^{100}Mo

$$^{100}Mo(\gamma,n+p)^{98m}Nb$$

Q-value (keV): -180103.4 Threshold (keV): 180103.4

$$^{99m}Nb \xrightarrow[51.3\ \mathrm{m}]{\beta-} {}^{98}Mo$$

Molybdenum-98 daughter is stable

Production of ^{98}Nb via gamma, neutron+proton reaction with ^{100}Mo

$$^{100}Mo(\gamma,n+p)^{98}Nb$$

Q-value (keV): -18019.4 Threshold (keV): 18021.15

$$^{98}Nb \xrightarrow[2.86\,s]{\beta-} {}^{98}Mo$$

Molybdenum-98 daughter is stable

Production of ^{97}Nb via gamma, 2-neutron+proton reaction with ^{100}Mo

$$^{100}Mo(\gamma,2n+p)^{97}Nb$$

Q-value (keV): -24013.0 Threshold (keV): 24016.1

$$^{97}Nb \xrightarrow[72.1\,\mathrm{min}]{\beta-} {}^{97}Mo$$

Molybdenum-97 daughter is stable

Production of ^{97}Zr via gamma, neutron + 2 proton reaction with ^{100}Mo

$$^{100}Mo\left(\gamma, n+2p\right)^{97}Zr$$

Q-value (keV): -25890.3 Threshold (keV): 25890.3

$$^{97}Zr \xrightarrow[16.749\ \mathrm{h}]{\beta-} {}^{97}Nb \xrightarrow[72.1\ \mathrm{m}]{\beta-} {}^{97}Mo$$

Molybdenum-97 daughter is stable

Production of ^{98}Nb via gamma, deuterium reaction with ^{100}Mo

$$^{100}Mo\left(\gamma, \mathrm{d}\right)^{98m}Nb$$

Q-value (keV): -15878.8 Threshold (keV): 15878.8

$$^{98m}Nb \xrightarrow[51.3\ \mathrm{min}]{\beta-} {}^{98}Mo$$

Molybdenum-98 daughter is stable

Production of ^{98}Nb via gamma, deuterium reaction with ^{100}Mo

$$^{100}Mo\left(\gamma, \mathrm{d}\right)^{98}Nb$$

Q-value (keV): -15794.84 Threshold (keV): 15796.18

$$^{98}Nb \xrightarrow[2.86\,s]{\beta-} {}^{98}Mo$$

Molybdenum-98 daughter is stable

Production of ^{97m}Nb via gamma, tritium reaction with ^{100}Mo

$$^{100}Mo\left(\gamma, t\right)^{97m}Nb$$

Q-value (keV): -16274.5 Threshold (keV): 16274.5

$$^{97m}Nb \xrightarrow[58.7\,s]{IT} {}^{97}Nb \xrightarrow[72.1\mathrm{min}]{\beta-} {}^{97}Mo$$

Molybdenum-97 daughter is stable

Production of ^{97}Nb via gamma, tritium reaction with ^{100}Mo

$$^{100}Mo(\gamma,t)^{97}Nb$$

Q-value (keV): -15531.2 Threshold (keV): 15532.5

$$^{97}Nb \xrightarrow[72.1\,\mathrm{min}]{\beta-} {}^{97}Mo$$

Molybdenum-97 daughter is stable

Production of ^{96}Zr via gamma, ^{3}He reaction with ^{100}Mo

$$^{100}Mo(\gamma,{}^{3}He)^{97}Zr$$

Q-value (keV): -18172.3 Threshold (keV): 18172.3

$$^{97}Zr \xrightarrow[16.749\ \mathrm{h}]{\beta-} {}^{97}Nb \xrightarrow[72.1\,\mathrm{min}]{\beta-} {}^{97}Mo$$

Molybdenum-97 daughter is stable

Production of ^{96}Zr via gamma, alpha reaction with ^{100}Mo

$$^{100}Mo(\gamma,\alpha)^{96}Zr$$

Q-value (keV): -3169.79 Threshold (keV): 3169.84

Zirconium-96 daughter is stable

---

^{98}Mo Reactions

Production of ^{97}Mo via photo-neutron reaction with ^{98}Mo

$$^{98}Mo(\gamma,n)^{97}Mo$$

Q-value (keV): -8642.6 Threshold (keV): 8643.009

Molybdenum-97 daughter is stable

Production of ^{96}Mo via gamma, 2-neutron reaction with ^{98}Mo

$$^{98}Mo(\gamma,2n)^{96}Mo$$

Q-value (keV): -15463.85 Threshold (keV): 15465.159

Molybdenum-96 daughter is stable

Production of ^{95}Mo via gamma, 3-neutron reaction with ^{98}Mo

$$^{98}Mo(\gamma,3n)^{95}Mo$$

Q-value (keV): -24618.18 Threshold (keV): 24621.5

Molybdenum-95 daughter is stable

Production of ^{97m}Nb via gamma, proton reaction with ^{98}Mo

$$^{98}Mo(\gamma,p)^{97m}Nb$$

Q-value (keV): -10539.1 Threshold (keV): 10539.1

$$^{97m}Nb \xrightarrow[58.7\ \mathrm{s}]{\beta-} {}^{97}Nb \xrightarrow[72.1\ \mathrm{m}]{\beta-} {}^{97}Mo$$

Molybdenum-97 daughter is stable

Production of ^{97}Nb via gamma, proton reaction with ^{98}Mo

$$^{98}Mo(\gamma, p)^{97}Nb$$

Q-value (keV): -9795.72 Threshold (keV): 9796.25

$$^{97}Nb \xrightarrow[72.1\text{min}]{\beta-} {}^{97}Mo$$

Molybdenum-97 daughter is stable

Production of ^{96}Zr via gamma, proton reaction with ^{98}Mo

$$^{98}Mo(\gamma, 2p)^{96}Zr$$

Q-value (keV): -17248.2 Threshold (keV): 17248.2

Zirconium-96 daughter is stable

Production of ^{96}Nb via gamma-neutron+proton reaction with ^{98}Mo

$$^{98}Mo(\gamma, n+p)^{96}Nb$$

Q-value (keV): -17868.3 Threshold (keV): 17870.05

$$^{96}Nb \xrightarrow[23.35h]{\beta-} {}^{96}Mo$$

Molybdenum-96 daughter is stable

Production of ^{95m}Nb via gamma - neutron + 2 proton reaction with ^{98}Mo

$$^{98}Mo(\gamma, 2n+p)^{95m}Nb$$

Q-value (keV): -24997.1 Threshold (keV): 24997.1

$$^{95m}Nb \xrightarrow[3.61\text{ d}]{\beta-} \begin{cases} \xrightarrow{94.4\%} {}^{95}Nb \xrightarrow[34.99\text{ d}]{\beta-} {}^{95}Mo \\ \xrightarrow{5.6\%} {}^{95}Mo \end{cases}$$

Molybdenum-95 daughter is stable

Production of ^{95}Nb via gamma-2-neutron+proton reaction with ^{98}Mo

$$^{98}Mo\left(\gamma,2n+p\right)^{95}Nb$$

Q-value (keV): -24761.398 Threshold (keV): 24764.756

$$^{95}Nb \xrightarrow[34.99\ \mathrm{d}]{\beta-} {}^{95}Mo$$

Molybdenum-95 daughter is stable

Production of ^{94m}Nb via gamma-3-neutron+proton reaction with ^{98}Mo

$$^{98}Mo\left(\gamma,3n+p\right)^{94m}Nb$$

Q-value (keV): -33289.5 Threshold (keV): 33289.5

$$^{94m}Nb \xrightarrow[3.61\ \mathrm{d}]{\beta-} \begin{cases} \xrightarrow[99.5\%]{} {}^{94}Nb \xrightarrow[2.03\mathrm{E}4\ \mathrm{y}]{\beta-} {}^{94}Mo \\ \xrightarrow[0.5\%]{} {}^{94}Mo \end{cases}$$

Molybdenum-94 daughter is stable

Production of ^{94}Nb via gamma-3-neutron+proton reaction with ^{98}Mo

$$^{98}Mo\left(\gamma,3n+p\right)^{94}Nb$$

Q-value (keV): -33248.57 Threshold (keV): 33254.63

$$^{94}Nb \xrightarrow[2.03E+4y]{\beta-} {}^{94}Mo$$

Molybdenum-94 daughter is stable

Production of ^{95}Zr via gamma, neutron+2-proton reaction with ^{98}Mo

$$^{98}Mo\left(\gamma, n+2p\right)^{95}Zr$$

Q-value (keV): -25102.55 Threshold (keV): 25106.0

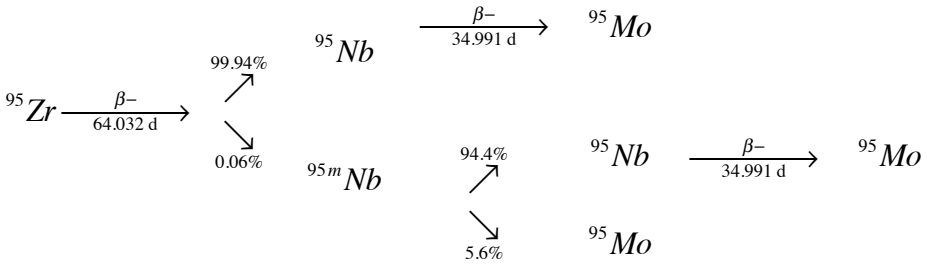

Molybdenum-95 daughter is stable

Production of ^{96}Nb via gamma-deuterium reaction with ^{98}Mo

$$^{98}Mo\left(\gamma, \mathrm{d}\right)^{96}Nb$$

Q-value (keV): -15643.74 Threshold (keV): 15645.08

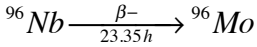

Molybdenum-96 daughter is stable

Production of ^{95m}Nb via gamma, tritium reaction with ^{98}Mo

$$^{98}Mo\left(\gamma, \mathrm{t}\right)^{95m}Nb$$

Q-value (keV): -16515.3 Threshold (keV): 16515.3

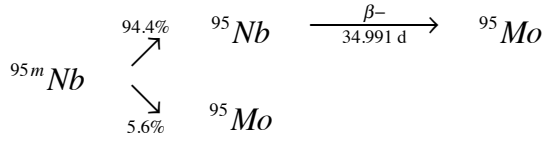

Molybdenum-95 daughter is stable

Production of ^{95}Nb via gamma, tritium reaction with ^{98}Mo

$$^{98}Mo(\gamma,\mathrm{t})\,^{95}Nb$$

Q-value (keV): -16279.592 Threshold (keV): 16281.043

$$^{95}Nb \xrightarrow[35\,d]{\beta-} {}^{95}Mo$$

Molybdenum-95 daughter is stable

Production of ^{95}Zr via gamma-^{3}He reaction with ^{98}Mo

$$^{98}Mo(\gamma,{}^{3}He)\,^{95}Zr$$

Q-value (keV): -17384.5 Threshold (keV): 17384.5

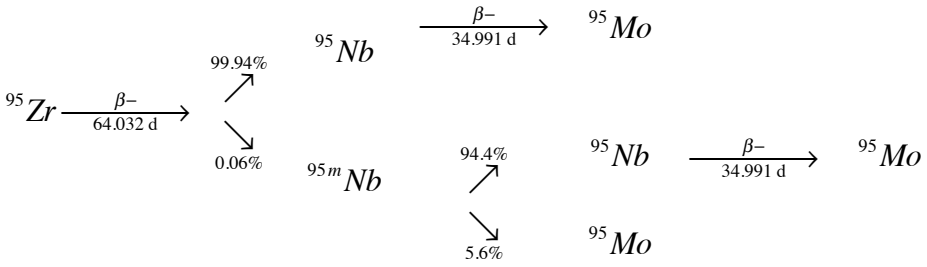

Molybdenum-95 daughter is stable

Production of ^{94}Zr via gamma-alpha reaction with ^{98}Mo

$$^{98}Mo(\gamma,\alpha)\,^{94}Zr$$

Q-value (keV): -3268.86 Threshold (keV): 3268.92

Zirconium-94 daughter is stable

---

^{97}Mo Reactions

Production of ^{96}Mo via photo-neutron reaction with ^{97}Mo

$$^{97}Mo(\gamma,n)^{96}Mo$$

Q-value (keV): -6821.25 Threshold (keV): 6821.507

Molybdenum-96 daughter is stable

Production of ^{95}Mo via gamma, 2-neutron reaction with ^{97}Mo

$$^{97}Mo(\gamma,2n)^{95}Mo$$

Q-value (keV): -15975.57 Threshold (keV): 15976.982

Molybdenum-95 daughter is stable

Production of ^{94}Mo via gamma, 3-neutron reaction with ^{97}Mo

$$^{97}Mo(\gamma,3n)^{94}Mo$$

Q-value (keV): -23344.68 Threshold (keV): 23347.695

Molybdenum-94 daughter is stable

Production of ^{96}Nb via gamma, proton reaction with ^{97}Mo

$$^{97}Mo(\gamma,\mathrm{p})^{96}Nb$$

Q-value (keV): -9225.7 Threshold (keV): 9226.17

$$^{96}Nb \xrightarrow[23.35h]{\beta-} {}^{96}Mo$$

Molybdenum-96 daughter is stable

Production of ^{95}Zr via gamma, 2-proton reaction with ^{97}Mo

$$^{97}Mo(\gamma,2p)^{95}Zr$$

Q-value (keV): -16459.94 Threshold (keV): 16461.44

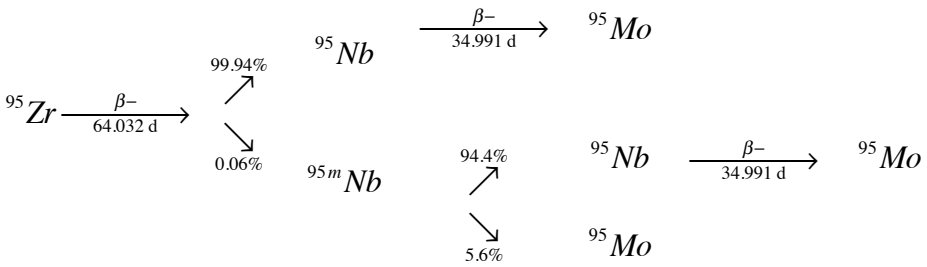

Molybdenum-95 daughter is stable

Production of ^{95m}Nb via gamma, neutron + proton reaction with ^{97}Mo

$$^{97}Mo(\gamma,\mathrm{n+p})^{95m}Nb$$

Q-value (keV): -16354.5 Threshold (keV): 16354.5

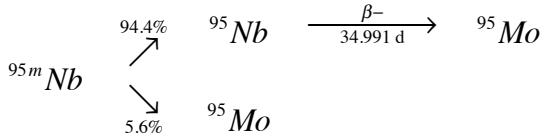

Molybdenum-95 daughter is stable Production of ^{95}Nb via gamma, neutron + proton reaction with ^{97}Mo

$$^{97}Mo(\gamma,\mathrm{n+p})^{95}Nb$$

Q-value (keV): -16118.794 Threshold (keV): 16120.231

$$^{95}Nb \xrightarrow[35d]{\beta-} {}^{95}Mo$$

Molybdenum-95 daughter is stable

Production of ^{94m}Nb via gamma, 2-neutron+proton reaction with ^{97}Mo

$$^{97}Mo\left(\gamma,2n+p\right)^{94m}Nb$$

Q-value (keV): -24646.9 Threshold (keV): 24646.9

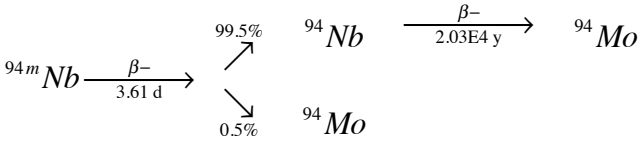

Molybdenum-94 daughter is stable

Production of ^{94}Nb via gamma, 2-neutron+proton reaction with ^{97}Mo

$$^{97}Mo\left(\gamma,2n+p\right)^{94}Nb$$

Q-value (keV): -24605.97 Threshold (keV): 24609.32

$$^{94}Nb \xrightarrow[2.03E+4\,y]{\beta-} {}^{94}Mo$$

Molybdenum-94 daughter is stable

Production of ^{94}Zr via gamma, neutron+2-proton reaction with ^{97}Mo

$$^{97}Mo\left(\gamma,\mathrm{n}+2\mathrm{p}\right)^{94}Zr$$

Q-value (keV): -22921.92 Threshold (keV): 22924.83

Zirconium-94 daughter is stable

Production of ^{95m}Nb via gamma, deuterium reaction with ^{97}Mo

$$^{97}Mo(\gamma,\mathrm{d})^{95m}Nb$$

Q-value (keV): -14129.9 Threshold (keV): 14129.9

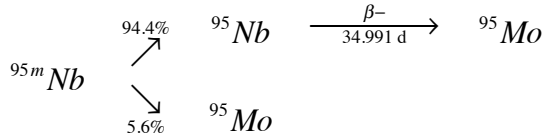

Molybdenum-95 daughter is stable

Production of ^{95}Nb via gamma, deuterium reaction with ^{97}Mo

$$^{97}Mo(\gamma,\mathrm{d})^{95}Nb$$

Q-value (keV): -13894.228 Threshold (keV): 13895.296

$$^{95}Nb \xrightarrow[35\,d]{\beta-} {}^{95}Mo$$

Molybdenum-95 daughter is stable

Production of ^{94m}Nb via gamma, tritium reaction with ^{97}Mo

$$^{97}Mo(\gamma,\mathrm{t})^{94m}Nb$$

Q-value (keV): -16165.0 Threshold (keV): 16165.0

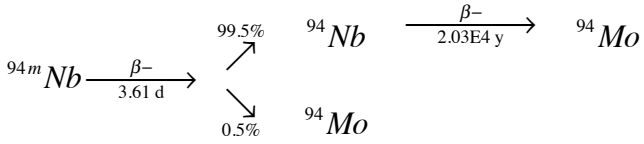

Molybdenum-94 daughter is stable

Production of ^{94}Nb via gamma, tritium reaction with ^{97}Mo

$$^{97}Mo(\gamma,\mathrm{t})\,^{94}Nb$$

Q-value (keV): -16124.16 Threshold (keV): 16125.6

$$^{94}Nb \xrightarrow[2.03E+4\,y]{\beta-} {}^{94}Mo$$

Molybdenum-94 daughter is stable

Production of ^{94}Zr via gamma, ^{3}He reaction with ^{97}Mo

$$^{97}Mo(\gamma,{}^{3}He)\,^{94}Zr$$

Q-value (keV): -2845.79 Threshold (keV): 2845.83

Zirconium-94 is stable

Production of ^{93}Zr via gamma, alpha reaction with ^{97}Mo

$$^{97}Mo(\gamma,\alpha)\,^{93}Zr$$

Q-value (keV): -2845.79 Threshold (keV): 2845.83

$$^{93}Zr \xrightarrow[1.6E+6\,y]{\beta-} {}^{93}Nb$$

Nobium-93 daughter is stable

---

^{96}Mo Reactions

Production of ^{95}Mo via photo-neutron reaction with ^{96}Mo

$$^{96}Mo(\gamma,n)^{95}Mo$$

Q-value (keV): -9154.32 Threshold (keV): 9154.789

Molybdenum-95 daughter is stable

Production of ^{94}Mo via gamma, 2-neutron reaction with ^{96}Mo

$$^{96}Mo(\gamma,2n)^{94}Mo$$

Q-value (keV): -16523.42 Threshold (keV): 16524.947

Molybdenum-94 daughter is stable

Production of ^{93m}Mo via gamma, 3-neutron reaction with ^{96}Mo

$$^{96}Mo(\gamma,3n)^{93m}Mo$$

Q-value (keV): -26201.266 Threshold (keV): 26205.104

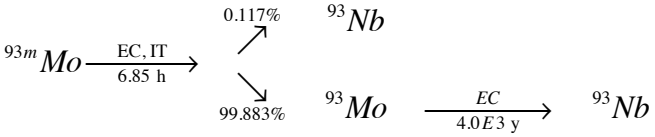

Niobium-93 daughter is stable

Production of ^{93}Mo via gamma, 3-neutron reaction with ^{96}Mo

$$^{96}Mo(\gamma,3n)^{93}Mo$$

Q-value (keV): -26201.266 Threshold (keV): 26205.104

$$^{93}Mo \xrightarrow[4.0E+3y]{EC} {}^{93}Nb$$

Niobium-93 daughter is stable

Production of ^{95m}Nb via gamma, proton reaction with ^{96}Mo

$$^{96}Mo(\gamma,\mathrm{p})^{95m}Nb$$

Q-value (keV): -9533.23 Threshold (keV): 9533.23

$$^{95m}Nb \begin{cases} \xrightarrow{94.4\%} {}^{95}Nb \xrightarrow[34.991\ \mathrm{d}]{\beta-} {}^{95}Mo \\ \xrightarrow{5.6\%} {}^{95}Mo \end{cases}$$

Molybdenum-95 daughter is stable

Production of ^{95}Nb via gamma, proton reaction with ^{96}Mo

$$^{96}Mo(\gamma,\mathrm{p})^{95}Nb$$

Q-value (keV): -9297.54 Threshold (keV): 9298.023

$$^{95}Nb \xrightarrow[35d]{\beta-} {}^{95}Mo$$

Molybdenum-95 daughter is stable

Production of ^{94}Zr via gamma, 2-proton reaction with ^{96}Mo

$$^{96}Mo(\gamma,2\mathrm{p})^{94}Zr$$

Q-value (keV): -16100.67 Threshold (keV): 16102.12

Zirconium-94 daughter is stable

Production of ^{94m}Nb via gamma, neutron+proton reaction with ^{96}Mo

$$^{96}Mo\left(\gamma,n+p\right)^{94m}Nb$$

Q-value (keV): -17825.6 Threshold (keV): 17825.6

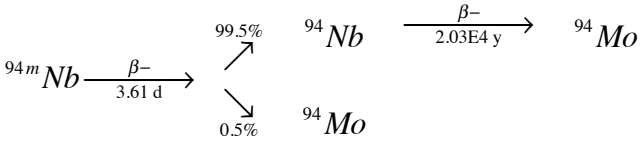

Molybdenum-94 daughter is stable

Production of ^{94}Nb via gamma, neutron+proton reaction with ^{96}Mo

$$^{96}Mo\left(\gamma,n+p\right)^{94}Nb$$

Q-value (keV): -17784.7 Threshold (keV): 17786.47

$$^{94}Nb \xrightarrow[2.03E+4\,y]{\beta-} {}^{94}Mo$$

Molybdenum-94 daughter is stable

Production of ^{93m}Nb via gamma, 2-neutron+proton reaction with ^{96}Mo

$$^{96}Mo\left(\gamma,2n+p\right)^{93m}Nb$$

Q-value (keV): -25043.0 Threshold (keV): 25043.0

$$^{93m}Nb \xrightarrow[16.12\ \mathrm{y}]{IT} {}^{93}Nb$$

Niobium-93 daughter is stable

Production of ^{93}Nb via gamma, 2-neutron+proton reaction with ^{96}Mo

$$^{96}Mo\left(\gamma,2n+p\right)^{93}Nb$$

Q-value (keV): -25012.25 Threshold (keV): 25015.75

Niobium-93 daughter is stable

Production of ^{93}Zr via gamma, neutron+2-proton reaction with ^{96}Mo

$$^{96}Mo\left(\gamma,\mathrm{n}+2p\right)^{93}Zr$$

Q-value (keV): -24320.2 Threshold (keV): 24323.51

$$^{93}Zr \xrightarrow[1.6E+6\,y]{\beta-} {}^{93}Nb$$

Nobium-93 daughter is stable

Production of ^{94m}Nb via gamma, deuterium reaction with ^{96}Mo

$$^{96}Mo\left(\gamma,\mathrm{d}\right)^{94m}Nb$$

Q-value (keV): -15560.14 Threshold (keV): 15561.49

$$^{94m}Nb \xrightarrow[3.61\ \mathrm{d}]{\beta-} \begin{cases} \xrightarrow{99.5\%} {}^{94}Nb \xrightarrow[2.03\mathrm{E}4\ \mathrm{y}]{\beta-} {}^{94}Mo \\ \xrightarrow{0.5\%} {}^{94}Mo \end{cases}$$

Molybdenum-94 daughter is stable

Production of ^{94}Nb via gamma, deuterium reaction with ^{96}Mo

$$^{96}Mo(\gamma,\mathrm{d})^{94}Nb$$

Q-value (keV): -15560.14 Threshold (keV): 15561.49

$$^{94}Nb \xrightarrow[2.03E+4\,y]{\beta-} {}^{94}Mo$$

Molybdenum-94 daughter is stable

Production of ^{93m}Nb via gamma, 2-tritium reaction with ^{96}Mo

$$^{96}Mo(\gamma,t)^{93m}Nb$$

Q-value (keV): -16561.2 Threshold (keV): 16561.2

$$^{93m}Nb \xrightarrow[16.12\ \mathrm{y}]{IT} {}^{93}Nb$$

Niobium-93 daughter is stable

Production of ^{93}Nb via gamma, 2-tritium reaction with ^{96}Mo

$$^{96}Mo(\gamma,t)^{93}Nb$$

Q-value (keV): -16530.45 Threshold (keV): 16531.98

Niobium-93 daughter is stable

Production of ^{93}Zr via gamma, alpha reaction with ^{96}Mo

$$^{96}Mo(\gamma,{}^{3}He)^{93}Zr$$

Q-value (keV): -16602.1 Threshold (keV): 16602.1

$$^{93}Zr \xrightarrow[1.61E6\ \mathrm{y}]{\beta-} {}^{93}Nb$$

Niobium-93 daughter is stable

Production of ^{92}Zr via gamma, alpha reaction with ^{96}Mo

$$^{96}Mo(\gamma,\alpha)^{92}Zr$$

Q-value (keV): -2758.91 Threshold (keV): 2758.95

Zirconium-92 daughter is stable

^{95}Mo Reactions

Production of ^{94}Mo via photo-neutron reaction with ^{95}Mo

$$^{95}Mo(\gamma,n)^{94}Mo$$

Q-value (keV): -7369.1 Threshold (keV): 7369.407

Molybdenum-94 daughter is stable

Production of ^{93m}Mo via gamma, 2-neutron reaction with ^{95}Mo

$$^{95}Mo(\gamma,2n)^{93m}Mo$$

Q-value (keV): -19471.9 Threshold (keV): 19471.9

$$^{93m}Mo \xrightarrow[6.85\ \text{h}]{\text{EC, IT}} \begin{cases} \xrightarrow{0.117\%} {}^{93}Nb \\ \xrightarrow{99.883\%} {}^{93}Mo \xrightarrow[4.0E3\ \text{y}]{EC} {}^{93}Nb \end{cases}$$

Niobium-93 daughter is stable

Production of ^{93}Mo via gamma, 2-neutron reaction with ^{95}Mo

$$^{95}Mo(\gamma,2n)^{93}Mo$$

Q-value (keV): -17046.94 Threshold (keV): 17048.582

$$^{93}Mo \xrightarrow[4.0E+3y]{EC} {}^{93}Nb$$

Niobium-93 daughter is stable

Production of ^{92}Mo via gamma, 3-neutron reaction with ^{95}Mo

$$^{95}Mo(\gamma,3n)^{92}Mo$$

Q-value (keV): -25116.758 Threshold (keV): 25120.322

Molybdenum-92 daughter is stable

Production of ^{94m}Nb via gamma, proton reaction with ^{95}Mo

$$^{95}Mo(\gamma,p)^{94m}Nb$$

Q-value (keV): -8671.28 Threshold (keV): 8671.28

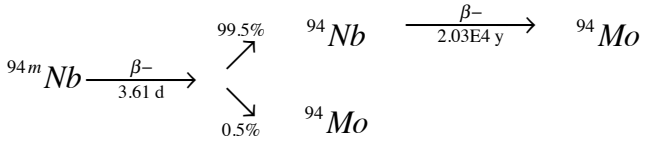

Molybdenum-94 daughter is stable

Production of ^{94}Nb via gamma, proton reaction with ^{95}Mo

$$^{95}Mo(\gamma,p)^{94}Nb$$

Q-value (keV): -8630.39 Threshold (keV): 8630.39

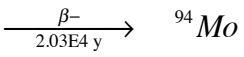

Molybdenum-94 daughter is stable

Production of ^{93}Zr via gamma, 2-proton reaction with ^{95}Mo

$$^{95}Mo\left(\gamma,2p\right)^{93}Zr$$

Q-value (keV): -15165.88 Threshold (keV): 15167.18

$$^{93}Zr \xrightarrow[1.6E+6\,y]{\beta-} {}^{93}Nb$$

Nobium-93 daughter is stable

Production of ^{93m}Nb via gamma, neutron + proton reaction with ^{95}Mo

$$^{95}Mo\left(\gamma,n+p\right)^{93m}Nb$$

Q-value (keV): -15888.7 Threshold (keV): 15888.7

$$^{93m}Nb \xrightarrow[16.12\ \mathrm{y}]{IT} {}^{93}Nb$$

Nobium-93 daughter is stable

Production of ^{93}Nb via gamma, neutron + proton reaction with ^{95}Mo

$$^{95}Mo\left(\gamma,n+p\right)^{93}Nb$$

Q-value (keV): -15857.9 Threshold (keV): 15857.9

Nobium-93 daughter is stable

Production of ^{92m}Nb via gamma, 2-neutron + proton reaction with ^{95}Mo

$$^{95}Mo\left(\gamma,2n+p\right)^{92m}Nb$$

Q-value (keV): -24824.0 Threshold (keV): 24824.0

$$^{92m}Nb \xrightarrow[10.15\ \mathrm{d}]{EC+,\beta+} {}^{92}Zr$$

Zirconium-92 daughter is stable

Production of ^{92}Nb via gamma, 2-neutron + proton reaction with ^{95}Mo

$$^{95}Mo\left(\gamma,2n+p\right)^{92}Nb$$

Q-value (keV): -24688.5 Threshold (keV): 24688.5

$$^{92}Nb \xrightarrow[13.47\,E{+}7\ \text{y}]{EC+} {}^{92}Zr$$

Zirconium-92 daughter is stable

Production of ^{92}Zr via gamma, neutron+2-proton reaction with ^{95}Mo

$$^{95}Mo\left(\gamma,\mathrm{n}+2\mathrm{p}\right)^{92}Zr$$

Q-value (keV): -21900.25 Threshold (keV): 21902.96

Zirconium-92 daughter is stable

Production of ^{93m}Nb via gamma, deuterium reaction with ^{95}Mo

$$^{95}Mo\left(\gamma,d\right)^{93m}Nb$$

Q-value (keV): -13664.1 Threshold (keV): 13664.1

$$^{93m}Nb \xrightarrow[16.12\ \text{y}]{IT} {}^{93}Nb$$

Niobium-93 daughter is stable

Production of ^{93}Nb via gamma, deuterium reaction with ^{95}Mo

$$^{95}Mo\left(\gamma,d\right)^{93}Nb$$

Q-value (keV): -13633.36 Threshold (keV): 13634.41

Niobium-93 daughter is stable

Production of ^{92}Nb via gamma, tritium reaction with ^{95}Mo

$$^{95}Mo(\gamma,\mathrm{t})\,^{92}Nb$$

Q-value (keV): -16206.68 Threshold (keV): 16208.17

$$^{92}Nb \xrightarrow[3.47E+7\,y]{EC} {}^{92}Zr$$

Zirconium-92 daughter is stable

Production of ^{92}Zr via gamma, alpha reaction with ^{95}Mo

$$^{95}Mo(\gamma,{}^{3}He)\,^{92}Zr$$

Q-value (keV): -14182.2 Threshold (keV): 14182.2

Zirconium-92 daughter is stable

Production of ^{91}Zr via gamma, alpha reaction with ^{95}Mo

$$^{95}Mo(\gamma,\alpha)\,^{91}Zr$$

Q-value (keV): -2239.38 Threshold (keV): 2239.41

Zirconium-91 daughter is stable

---

^{94}Mo Reactions

Production of ^{93m}Mo via photo-neutron reaction with ^{94}Mo

$$^{94}Mo(\gamma,n)^{93m}Mo$$

Q-value (keV): -12102.8 Threshold (keV): 12102.8

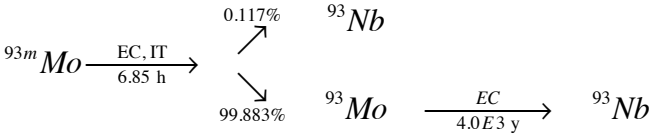

Niobium-93 daughter is stable

Production of ^{93}Mo via photo-neutron reaction with ^{94}Mo

$$^{94}Mo(\gamma,n)^{93}Mo$$

Q-value (keV): -9677.84 Threshold (keV): 9678.375

$$^{93}Mo \xrightarrow[4.0E+3y]{EC} {}^{93}Nb$$

Niobium-93 daughter is stable

Production of ^{92}Mo via gamma, 2-neutron reaction with ^{94}Mo

$$^{94}Mo(\gamma,2n)^{92}Mo$$

Q-value (keV): -17747.65 Threshold (keV): 17749.45

Molybdenum-92 daughter is stable

Production of ^{91m}Mo via gamma, 3-neutron reaction with ^{94}Mo

$$^{94}Mo\left(\gamma,3n\right)^{91m}Mo$$

Q-value (keV): -30418.09 Threshold (keV): 30423.38

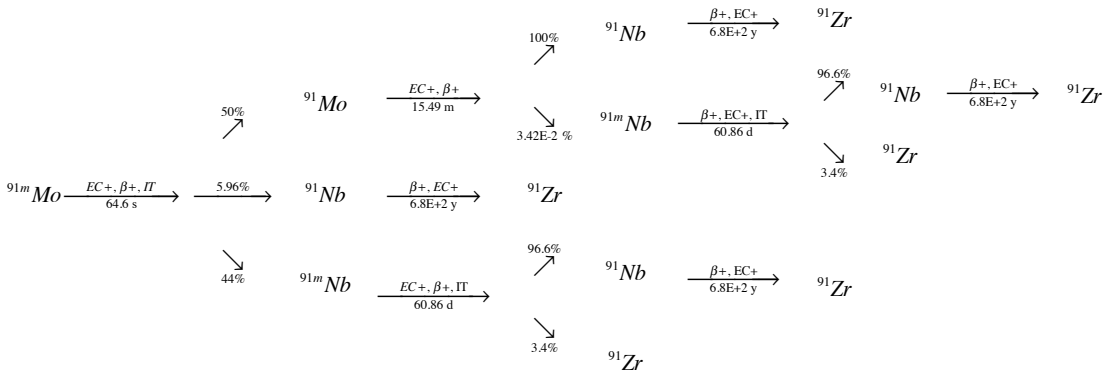

Zirconium-91 daughter is stable

Production of ^{91}Mo via gamma, 3-neutron reaction with ^{94}Mo

$$^{94}Mo\left(\gamma,3n\right)^{91}Mo$$

Q-value (keV): -30418.09 Threshold (keV): 30423.38

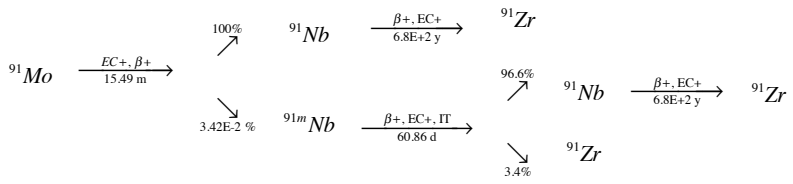

Zirconium-91 daughter is stable

Production of ^{93m}Nb via gamma, proton reaction with ^{94}Mo

$$^{94}Mo(\gamma,p)^{93m}Nb$$

Q-value (keV): -8519.6 Threshold (keV): 8519.6

$$^{93m}Nb \xrightarrow[16.12\ \mathrm{y}]{IT} {}^{93}Nb$$

Niobium-93 daughter is stable

Production of ^{93}Nb via gamma, proton reaction with ^{94}Mo

$$^{94}Mo(\gamma,p)^{93}Nb$$

Q-value (keV): -8488.83 Threshold (keV): 8489.24

Niobium-93 daughter is stable

Production of ^{92}Zr via gamma, 2-proton reaction with ^{94}Mo

$$^{94}Mo(\gamma,2\mathrm{p})^{92}Zr$$

Q-value (keV): -14531.15 Threshold (keV): 14532.36

Zirconium-92 daughter is stable

Production of ^{92m}Nb via gamma, neutron + proton reaction with ^{94}Mo

$$^{94}Mo(\gamma,n+p)^{92m}Nb$$

Q-value (keV): -17454.9 Threshold (keV): 17454.9

$$^{92m}Nb \xrightarrow[10.15\ \mathrm{d}]{EC+,\beta+} {}^{92}Zr$$

Zirconium-92 daughter is stable

Production of ^{92}Nb via gamma, neutron + proton reaction with ^{94}Mo

$$^{94}Mo(\gamma, n+p)^{92}Nb$$

Q-value (keV): -17319.38 Threshold (keV): 17321.1

$$^{92}Nb \xrightarrow[3.47E+7\,y]{EC} {}^{92}Zr$$

Zirconium-92 daughter is stable

Production of ^{91m}Nb via gamma, 2-neutron + proton reaction with ^{94}Mo

$$^{94}Mo(\gamma, 2n+p)^{91m}Nb$$

Q-value (keV): -25310.5 Threshold (keV): 25310.5

$$^{91m}Nb \xrightarrow[60.86\text{ d}]{EC+,\ \beta+,\ \text{IT}} \begin{cases} \xrightarrow{96.6\%} {}^{91}Nb \xrightarrow[6.8\text{E+2 y}]{\beta+,\ \text{EC+}} {}^{91}Zr \\ \xrightarrow{3.4\%} {}^{91}Zr \end{cases}$$

Zirconium-91 daughter is stable

Production of ^{91}Nb via gamma, 2-neutron + proton reaction with ^{94}Mo

$$^{94}Mo(\gamma, 2n+p)^{91}Nb$$

Q-value (keV): -25205.87 Threshold (keV): 25209.5

$$^{91}Nb \xrightarrow[680\,y]{\beta+} {}^{91}Zr$$

Zirconium-91 daughter is stable

Production of ^{91}Zr via gamma, neutron + 2-proton reaction with ^{94}Mo

$$^{94}Mo(\gamma, \mathrm{n}+2\mathrm{p})^{91}Zr$$

Q-value (keV): -23165.95 Threshold (keV): 23169.01

Zirconium-91 daughter is stable

Production of ^{92m}Nb via gamma, deuterium reaction with ^{94}Mo

$$^{94}Mo(\gamma, d)^{92m}Nb$$

Q-value (keV): -15230.3 Threshold (keV): 15230.3

$$^{92m}Nb \xrightarrow[10.15\ \mathrm{d}]{EC+,\beta+} {}^{92}Zr$$

Zirconium-92 daughter is stable

Production of ^{92}Nb via gamma, deuterium reaction with ^{94}Mo

$$^{94}Mo(\gamma, d)^{92}Nb$$

Q-value (keV): -15094.82 Threshold (keV): 15096.12

$$^{92}Nb \xrightarrow[3.47E+7\,y]{EC} {}^{92}Zr$$

Zirconium-92 daughter is stable

Production of ^{91m}Nb via gamma, tritium reaction with ^{94}Mo

$$^{94}Mo(\gamma,t)^{91m}Nb$$

Q-value (keV): -16828.7 Threshold (keV): 16828.7

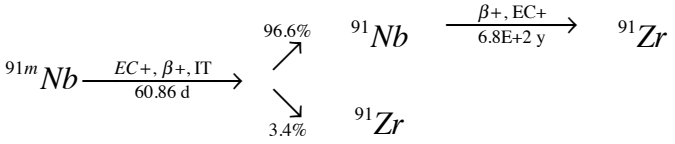

Zirconium-91 daughter is stable

Production of ^{91}Nb via gamma, tritium reaction with ^{94}Mo

$$^{94}Mo(\gamma,t)^{91}Nb$$

Q-value (keV): -16724.07 Threshold (keV): 16725.67

$$^{91}Nb \xrightarrow[680\,y]{\beta+} {}^{91}Zr$$

Zirconium-91 daughter is stable

Production of ^{91}Zr via gamma, ^{3}He reaction with ^{94}Mo

$$^{94}Mo(\gamma,{}^{3}He)^{91}Zr$$

Q-value (keV): -15447.9 Threshold (keV): 15447.9

Zirconium-90 daughter is stable

Production of ^{90}Zr via gamma, alpha reaction with ^{94}Mo

$$^{94}Mo(\gamma,\alpha)^{90}Zr$$

Q-value (keV): -2064.2 Threshold (keV): 2064.22

Zirconium-90 daughter is stable

---

^{92}Mo Reactions

Production of ^{91}Mo via photo-neutron reaction with ^{92}Mo

$$^{92}Mo(\gamma,n)^{91m}Mo$$

Q-value (keV): -13323.4 Threshold (keV): 13323.4

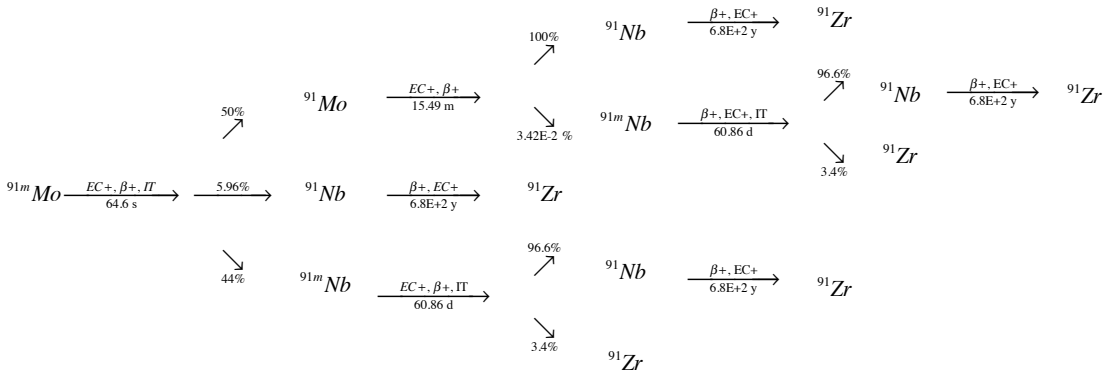

Zirconium-91 daughter is stable

Production of ^{91}Mo via photo-neutron reaction with ^{92}Mo

$$^{92}Mo(\gamma,n)^{91}Mo$$

Q-value (keV): -12670.4 Threshold (keV): 13323.4

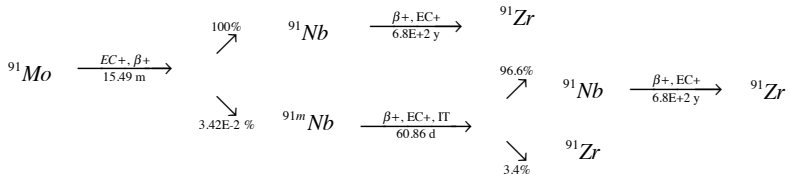

Zirconium-91 daughter is stable

Production of ^{90}Mo via gamma, 2-neutron reaction with ^{92}Mo

$$^{92}Mo\left(\gamma,2n\right)^{90}Mo$$

Q-value (keV): -22777.57 Threshold (keV): 22780.6

$$^{90}Mo \xrightarrow[5.67h]{\beta+} {}^{90}Nb \xrightarrow[14.6h]{\beta+} {}^{90}Zr$$

Zirconium-90 daughter is stable

Production of ^{89m}Mo via gamma, 3-neutron reaction with ^{92}Mo

$$^{92}Mo\left(\gamma,3n\right)^{89m}Mo$$

Q-value (keV): -36006.85 Threshold (keV): 36014.41

$$^{89m}Mo \xrightarrow[190\ \text{ms}]{\text{IT}} {}^{89}Mo \begin{cases} \xrightarrow{0.9\%} {}^{89m}Nb \xrightarrow[66\ \text{m}]{\beta+,\ \text{EC}+} {}^{89}Zr \xrightarrow[78.41\ \text{h}]{\beta+,\ \text{EC}+} {}^{89}Y \\ \xrightarrow{99.1\%} {}^{89}Nb \xrightarrow[2.03\ \text{h}]{\beta+,\ \text{EC}+} {}^{89}Zr \xrightarrow[78.41\ \text{h}]{\beta+,\ \text{EC}+} {}^{89}Y \end{cases}$$

Yttrium-89 daughter is stable

Production of ^{89}Mo via gamma, 3-neutron reaction with ^{92}Mo

$$^{92}Mo(\gamma,3n)^{89}Mo$$

Q-value (keV): -36006.85 Threshold (keV): 36006.85

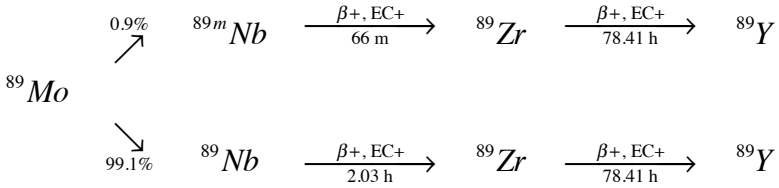

Yttrium-89 daughter is stable

Production of ^{91m}Nb via gamma, proton reaction with ^{92}Mo

$$^{92}Mo(\gamma,p)^{91m}Nb$$

Q-value (keV): -7562.82 Threshold (keV): 7562.82

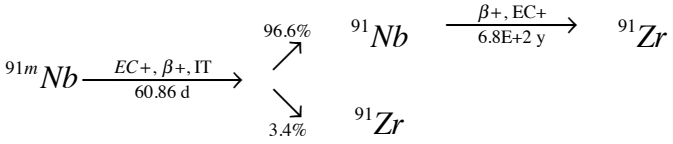

Zirconium-91 daughter is stable

Production of ^{91}Nb via gamma, proton reaction with ^{92}Mo

$$^{92}Mo(\gamma,p)^{91}Nb$$

Q-value (keV): -7458.22 Threshold (keV): 7458.54

$$^{91}Nb \xrightarrow[680\,y]{\beta+} {}^{91}Zr$$

Zirconium-91 daughter is stable

Production of ^{90m}Zr via gamma, 2-proton reaction with ^{92}Mo

$$^{92}Mo\left(\gamma,2\mathrm{p}\right)^{90m}Zr$$

Q-value (keV): -14931.2 Threshold (keV): 14931.2

$$^{90m}Zr \xrightarrow[809.2\mathrm{ms}]{\mathrm{IT}} {}^{90}Zr$$

Production of ^{90}Zr via gamma, 2-proton reaction with ^{92}Mo

$$^{92}Mo\left(\gamma,2\mathrm{p}\right)^{90}Zr$$

Q-value (keV): -12612.2 Threshold (keV): 12612.2

Zirconium-90 daughter is stable

Production of ^{89m}Y via gamma, 3-proton reaction with ^{92}Mo

$$^{92}Mo\left(\gamma,3\mathrm{p}\right)^{89m}Y$$

Q-value (keV): -21874.6 Threshold (keV): 21874.6

$$^{89m}Y \xrightarrow[15.663\ \mathrm{s}]{\mathrm{IT}} {}^{89}Y$$

Yttrium-89 daughter is stable

Production of ^{89}Y via gamma, 3-proton reaction with ^{92}Mo

$$^{92}Mo\left(\gamma,3\mathrm{p}\right)^{89}Y$$

Q-value (keV): -20965.6 Threshold (keV): 20965.6

Yttrium-89 daughter is stable

Production of ^{90m}Nb via gamma, neutron + proton reaction with ^{92}Mo

$$^{92}Mo\left(\gamma,n+p\right)^{90m}Nb$$

Q-value (keV): -19630.6 Threshold (keV): 19630.6

$$^{90m}Nb \xrightarrow[18.97\ \mathrm{s}]{\mathrm{IT}} {}^{90}Nb \xrightarrow[14.6\ \mathrm{h}]{\mathrm{EC},\beta+} {}^{90}Zr$$

Zirconium-90 daughter is stable

Production of ^{90}Nb via gamma, neutron + proton reaction with ^{92}Mo

$$^{92}Mo\left(\gamma,n+p\right)^{90}Nb$$

Q-value (keV): -19505.89 Threshold (keV): 19508.12

$$^{90}Nb \xrightarrow[14.6\ \mathrm{h}]{\mathrm{EC},\beta+} {}^{90}Zr$$

Zirconium-90 daughter is stable

Production of ^{89m}Nb via gamma, 2-neutron + proton reaction with ^{92}Mo

$$^{92}Mo\left(\gamma,2n+p\right)^{89m}Nb$$

Q-value (keV): -29649.0 Threshold (keV): 29649.0

$$^{89m}Nb \xrightarrow[66\,\mathrm{min}]{\beta+EC+} {}^{89}Zr \xrightarrow[78.41h]{\beta+} {}^{89}Y$$

Yttrium-89 daughter is stable

Production of ^{89}Nb via gamma, 2-neutron + proton reaction with ^{92}Mo

$$^{92}Mo\left(\gamma,2n+p\right)^{89}Nb$$

Q-value (keV): -29614.0 Threshold (keV): 29619.2

$$^{89}Nb \xrightarrow[2.03h]{\beta+} {}^{89}Zr \xrightarrow[78.41h]{\beta+} {}^{89}Y$$

Yttrium-89 daughter is stable

Production of ^{89m}Zr via gamma, neutron + 2-proton reaction with ^{92}Mo

$$^{92}Mo\left(\gamma,\mathrm{n}+2\mathrm{p}\right)^{89m}Zr$$

Q-value (keV): -25168.5 Threshold (keV): 25168.5

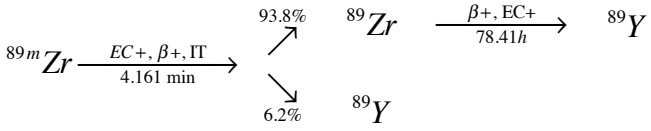

Yttrium-89 daughter is stable

Production of ^{89}Zr via gamma, neutron + 2-proton reaction with ^{92}Mo

$$^{92}Mo\left(\gamma,\mathrm{n}+2\mathrm{p}\right)^{89}Zr$$

Q-value (keV): -24580.7 Threshold (keV): 24584.22

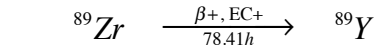

Yttrium-89 daughter is stable

Production of ^{90m}Nb via gamma, deuterium reaction with ^{92}Mo

$$^{92}Mo\left(\gamma,\mathrm{d}\right)^{90m}Nb$$

Q-value (keV): -17406.0 Threshold (keV): 17406.0

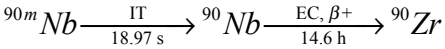

Zirconium-90 daughter is stable

Production of ^{90}Nb via gamma, deuterium reaction with ^{92}Mo

$$^{92}Mo\left(\gamma,\mathrm{d}\right)^{90}Nb$$

Q-value (keV): -17281.33 Threshold (keV): 17283.07

$$^{90}Nb \xrightarrow[14.6\,\mathrm{h}]{\mathrm{EC},\,\beta+} {}^{90}Zr$$

Zirconium-90 daughter is stable

Production of ^{89m}Nb via gamma, tritium reaction with ^{92}Mo

$$^{92}Mo\left(\gamma,\mathrm{t}\right)^{89m}Nb$$

Q-value (keV): -21167.2 Threshold (keV): 21167.2

$$^{89m}Nb \xrightarrow[66\,\mathrm{min}]{\beta+EC+} {}^{89}Zr \xrightarrow[78.41h]{\beta+} {}^{89}Y$$

Yttrium-89 daughter is stable

Production of ^{89}Nb via gamma, tritium reaction with ^{92}Mo

$$^{92}Mo\left(\gamma,t\right)^{89}Nb$$

Q-value (keV): -16724.07 Threshold (keV): 16725.67

$$^{89}Nb \xrightarrow[2.03h]{\beta+} {}^{89}Zr \xrightarrow[78.41h]{\beta+} {}^{89}Y$$

Yttrium-89 daughter is stable

Production of ^{89m}Zr via gamma, ^{3}He reaction with ^{92}Mo

$$^{92}Mo\left(\gamma,{}^{3}He\right)^{89m}Zr$$

Q-value (keV): -17450.5 Threshold (keV): 17450.5

$$^{89m}Zr \xrightarrow[4.161\ \text{min}]{EC+,\beta+,\text{IT}} \begin{cases} \xrightarrow{93.8\%} {}^{89}Zr \xrightarrow[78.41h]{\beta+,\text{EC+}} {}^{89}Y \\ \xrightarrow{6.2\%} {}^{89}Y \end{cases}$$

Yttrium-89 daughter is stable

Production of ^{89}Zr via gamma, ^{3}He reaction with ^{92}Mo

$$^{92}Mo\left(\gamma,{}^{3}He\right)^{89}Zr$$

Q-value (keV): -15447.9 Threshold (keV): 15447.9

$$^{89}Zr \xrightarrow[78.41h]{\beta+,\text{EC+}} {}^{89}Y$$

Yttrium-89 daughter is stable

Production of ^{88}Zr via gamma, alpha reaction with ^{92}Mo

$$^{92}Mo\left(\gamma,\alpha\right)^{88}Zr$$

Q-value (keV): -5604.41 Threshold (keV): 5604.59

$$^{88}Zr \xrightarrow[83.4d]{EC} {}^{88}Y \xrightarrow[106.627d]{EC+\beta+} {}^{88}Sr$$

Strontium-88 daughter is stable